UNIVERSITY OF OKLAHOMA

GRADUATE COLLEGE

Mathematical Optimization Models for Treatment Planning of Spatially Fractionated Radiation Therapy

A THESIS
SUBMITTED TO THE GRADUATE FACULTY

in partial fulfillment of the requirements for the
Degree of

MASTER OF SCIENCE

By
GRANT BENSON

Norman, Oklahoma
2025

Mathematical Optimization Models for Treatment Planning of Spatially Fractionated Radiation Therapy

A thesis approved for the School of Industrial and Systems Engineering by the committee consisting of:

Dr. M. Soheil Hemmati, Committee Chair
Assistant Professor, School of Industrial and Systems Engineering

Dr. Raghavendiran Boopathy, Member of Committee
Associate Professor, Radiation Oncology

Dr. Andres Gonzalez, Member of Committee
Associate Professor, School of Industrial and Systems Engineering

Dr. Rui Zhu, Member of Committee
Assistant Professor, School of Industrial and Systems Engineering

Abstract

Spatially Fractionated Radiation Therapy (SFRT) is an emerging approach in radiation oncology that has gained interest in recent years as an effective method for the treatment of large and bulky tumors. Rather than prescribing a consistent, high dose of radiation to the entire tumor volume, SFRT prescribes delivery of high doses of radiation to discrete spheres within the tumor. While clinical guidelines exist regarding sphere size and separation, currently there is no rigorously defined method that places these spheres within the tumor. Instead, treatment planners rely on their own experience to determine sphere locations, aiming to maximize the number of spheres while satisfying clinical constraints. This step is typically followed by fluence map optimization, the primary task in radiation therapy planning, where the intensity of the radiation "beamlets" is computed. This manual sphere placement process introduces variation in both the number of spheres placed and the locations of these spheres, which can result in inconsistent and suboptimal treatment plans with potentially unfavorable patient outcomes. In this thesis, we propose a novel mathematical optimization model that computes the optimal SFRT treatment plan that places the maximum number of spheres within the tumor by integrating an instance of the maximum independent set (MIS) problem within fluence map optimization. Our model places spheres within the tumor in the configuration that maximizes radiation dose to the tumor and minimizes radiation dose to healthy tissues. We conduct an experimental evaluation of our model using real imaging data provided by the National Cancer Institute through The Cancer Imaging Archive (TCIA). Our results demonstrate the effectiveness and flexibility of the proposed framework and its potential to assist clinicians in making more informed decisions that improve patient outcomes.

Acknowledgments

I would like to express my profound gratitude to my advisor, Dr. Soheil Hemmati. His enthusiasm, patience, and guidance throughout this journey has been fundamental to my success, both in and beyond the thesis. I commend him for going above and beyond the call of an advisor, ascending to the level of a friend and mentor whom I will cherish for the rest of my life: I promise to answer emails and texts.

I would also like to thank my committee members: Dr. Raghavendiran Boopathy, Dr. Andres Gonzalez, and Dr. Rui Zhu for their time and effort. Dr. Boopathy has been especially instrumental and helpful, always making time and offering guidance and insight. Additionally, Mansoor Khan has been extremely helpful, spending long hours meeting with me, providing important information, and processing patient data.

I would like to thank my friends who have supported me in this journey, both in and out of the ISE department. In particular, Jeorge and Kiana, my labmates, for listening to my rambling for a full year, and my roommates Cesar and Will, for enduring the slow decomposition of our apartment during busy research periods.

Finally and most importantly, I would like to thank my family for their love and support. All of my intelligence and curiosity are products of their work and love.

Contents

List of Figures

List of Tables

Chapter 1

Introduction

1.1 Cancer Background

Cancer remains one of the most pressing global health challenges of the 21st century. It refers to a group of diseases that are characterized by the uncontrolled growth and division of abnormal cells in the body. Such uncontrolled "proliferation" is often accompanied by an invasion of the surrounding tissues or spread to distant organs through the bloodstream or lymphatic system, which is known as cancer metastasis. Cancer encompasses over 200 distinct types, each with unique risk factors, biological behaviors, and treatment responses. Nearly half of all newly diagnosed cancer cases in the United States are attributed to breast, lung, bladder, prostate, and colorectal cancers combined [47].

Globally, an estimated 9.7 million people died from cancer in 2022, and there were roughly 20 million new cancer cases, with 2.7 million cases in North America alone [10, 16]. This high death toll makes cancer the leading cause of death for Americans under the age of 85, with 2,041,910 new cancer cases and 618,120 cancer deaths predicted in 2025 [46]. In the United States, half of all men and one third of all women will develop cancer during their lifetimes. This has led to monikers such as "the Pathology of the Century" [13, 37].

As our understanding of cancer has grown, we understand that many amenities of the modern age increase our risk of cancer, from obesity to smoking to pesticides to nuclear power, to even the CT scans that we use to help cure cancer; cancer is seen as a "product of modernity" [6, 13, 37].

The consequences of cancer are not limited to clinical outcomes; in addition to severely affecting patient's quality of life, it affects families and the society at large. Cancer patients

experience profound psychological, emotional, and financial distress, while survivors often face long-term complications and reduced quality of life. At the societal level, cancer imposes significant economic costs by straining healthcare systems and workforce productivity. In this context, interdisciplinary research that integrates biology, physics, and mathematics (along with other relevant disciplines from social sciences, epidemiology, and health policy making) is crucial for informing a wide array of approaches for cancer prevention, treatment, and survivorship. This thesis particularly focuses on building upon mathematical optimization models for treatment planning task of a modern radiation therapy technique.

1.1.1 Historical Overview of Cancer Treatment

Early Treatments Given that cancer has afflicted humanity for centuries, efforts to understand and treat the disease have been ongoing throughout history. The first recorded evidence of cancer identification and treatment comes from the Edwin Smith Papyrus (Figure 1.1) from 1500 BC in ancient Egypt, which depicts the surgical cauterization of a surface breast cancer tumor [2, 4, 34].

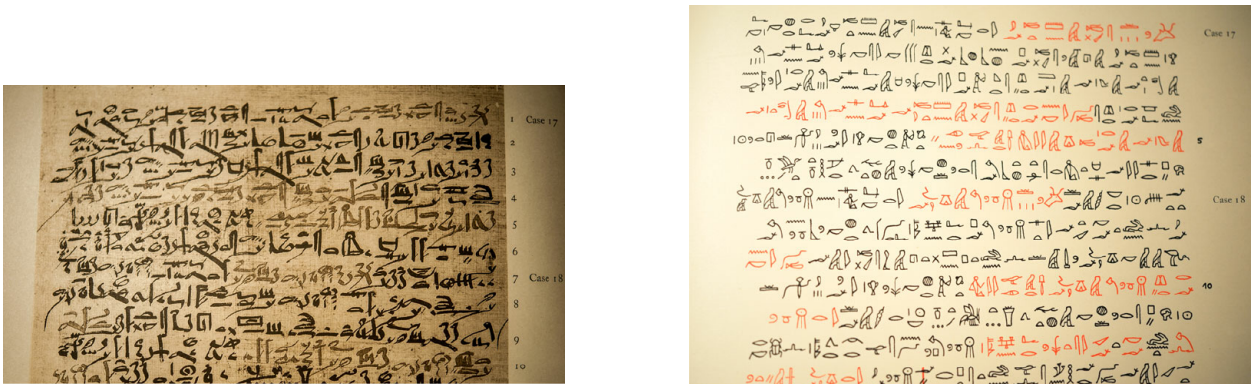

Figure 1.1: Sections of the Edwin Smith Papyrus, depicting ancient Egyptian medical cases and treatments [2].

Hippocrates attempted to understand the causes of Cancer in the 300s BC, integrating it into his theory of the four humors, which stated that infirmity is caused by imbalances in four bodily fluids: blood, yellow bile, black bile and phlegm. He theorized that cancer resulted from a buildup of black bile in a particular part of the body [26, 48, 50]. Hippocrates even coined the phrase *karkinos* (meaning crab in Greek, due to the way some tumors produced swollen veins, giving the appearance of a crab), which is the etymological root of the word cancer.

Hippocrates' theory of humors dominated European medicine for over a thousand years. The Roman physician Galen codified and expanded upon Hippocrates' work and differentiated between benign and malignant tumors, but cancer was often believed to be incurable until modern times [23, 41]. Early prescriptions for cancer generally involved a clean diet and cauterization. In a time before anesthesia, they would perform surgical removal if possible, and palliative care if not [19].

Later, starting in the Renaissance, some physicians began to move away from the humoral theory, and started to look at environmental factors as potential causes of cancer. Finally in the 1700s, the scientific method was applied to study carcinogenic effects of chemicals such as ash and soot [19]. The theory of humors declined during the enlightenment with the dawn of cell theory. This was a major turning point, as cancer came to be understood as a disease of the cells rather than of humors. As research progressed, multiple new theories emerged that tried to explain the causes of cancer, including that cancer was caused by trauma, parasites, or chronic irritation, but a true and deep understanding of cancer would not come until the 1960's, with the discovery of DNA and genetic mutation [48]. We now know that cancer is unregulated cell growth, caused by carcinogens, radiation, viruses, and genetics, through damage to genetic material.

However, treatment methods did not progress significantly until enlightenment scientists provided a deeper and more accurate understanding of anatomy. This development, along with the development of anesthesia, allowed for more sophisticated surgical tumor removals. After the enlightenment, the next truly groundbreaking advancement in cancer treatment would not come until the late 19th century. This was when X-rays were discovered, leading to the discovery of radioactivity and the development of radiotherapy [19].

Advancements in the 20th Century Marie Curie, upon discovering the way that radiation damaged organic tissue on a cellular level, recommended its use in oncology [28]. In 1896, X-rays were first used for treatment of breast cancer, but modern clinical use of radiotherapy began in 1920 due to advances in radiation therapy machinery and our understanding of the effect of radiation on the body [17, 36, 38].

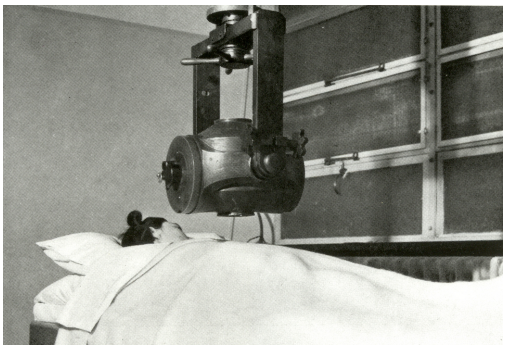

Figure 1.2: The first external beam radiotherapy device developed at Memorial Hospital (now Memorial Sloan Kettering Cancer Center) [1].

As seen in Figure 1.2, these early machines contained a radiation source in a shielded housing, and had an aperture that could be opened to dose a tumor with radiation. These early machines used X-rays or a radioactive isotope (such as Cobalt-60 or Radium-223), and were generally inaccurate and only able to deliver radiation from a single angle. Furthermore, our understanding of dosimetry was crude, so different patients could receive vastly different doses of radiation. One early metric for the length of time that a person should be dosed for was the redness of their skin as the radiation began to burn. They would simply deliver dose until the patient began to redden. This was a very crude metric, as skin sensitivity varies from person to person, so more sophisticated metrics were developed as radiation therapy matured that would ensure an accurate dose that resulted in less healthy tissue damage.

The 20th century saw many advancements in radiation therapy treatment planning, due to our advancing understanding of radiation, cell biology, and genetics. One of the most important early developments that reduced healthy tissue damage was Fractionation. Fractionation is a key part of what makes radiation therapy an effective treatment [36]. Different cells throughout the body are more or less sensitive to damage from radiation. Many cancer cells are more susceptible to radiation, and heal slower, than healthy tissues [36]. Thus, by dividing the dose into multiple "fractions" and delivering a fraction of the full prescribed dose through multiple treatment sessions, often lasting weeks, the healthy tissues are given time to heal, while the tumor atrophies [36].

Thanks to advances in genetics and our understanding of DNA's structure, we now know that radiation therapy works by targeting the cell's DNA and triggering single strand and double strand breaks in the structure of the DNA. This is done both through a direct hit to the DNA, which often triggers a double strand break in the DNA, and the creation of free radicals due to radiation exposure, which causes a reaction that damages the cell's DNA

and leads to cell death [7]. Due to the genomic instability of these damaged cells, they will die, ether through apoptosis, which is programmed cell death, Mitotic cell death, which is an error of cell division, necrosis, which is a swelling and breakdown of the cell membrane, senescence, which is the inability to proliferate, or autophagy, which is another programmed cell death where the cell digests itself [7]. Most cells will undergo apoptosis, although all of these cell death pathways can occur depending on the cellular context.

Despite developments in radiation therapy, surgery was generally the dominant approach throughout the 20th century. Radical surgery, that would remove large amounts of healthy tissue, was common because surgery was often ineffective if the tumor was advanced or if the surgeon failed to remove the entirety of the tumor [19]. These highly invasive procedures could have massive impacts on the patients quality of life, even if the surgery was successful.

The next great advancement in 20th century cancer treatment was Chemotherapy. Chemotherapy was developed in the 1940s, but it was not a targeted approach at the time. Many of these treatments had trouble targeting tumor cells and would cause damage to healthy tissues as well, which took a heavy toll on the patient. With greater research and greater understanding, more targeted approaches were developed in the late 20th century that allowed for more effective treatment that had less side effects, but the treatment was still accompanied by severe outcomes [14, 27].

Modern Era In the modern age, all of these treatment modalities can be used, and have been refined to be more effective and improve patient quality of life. In addition to these, new techniques have been introduced such as hormone therapy, adjuvant therapy, immunotherapy, and bone marrow transplants, aiming to inhibit cancer cell growth, trigger apoptosis (cell death) in the tumor, or otherwise inhibit proliferation of cancer cells [48].

One of the key features of modern cancer treatment is multi-modal treatment. Depending on the cancer site (and other pathological characteristics), a patient may receive an initial chemotherapy (called induction therapy) followed by radiation therapy. With more "localized" cancers (e.g., tumors in early stages), the patient may be eligible for surgery, but may also undergo post or pre-operative chemo or radiation therapy as an adjuvant treatment in order to maximize treatment effectiveness and patient quality of life [48]. Radiation therapy, in general, has been vastly improved in this century with more advanced imaging-guided procedures, more sophisticated machinery that allows for more accurate and precise radiation delivery, and the development of particle therapy that uses protons, electrons, or even neutrons, rather than just X-rays (photons). With WHO reporting that over half of all cancer patients will

need radiation therapy at some point during their treatment, this treatment modality has become an essential component of modern cancer management [40].

1.1.2 Current Radiation Therapy Techniques

Radiation Therapy has become one of the leading treatment modalities in recent years. Many forms of cancer can be cured with radiation therapy alone, including skin cancers, prostate carcinomas, lung carcinomas, cervix carcinomas, lymphomas, and head and neck carcinomas [7]. Many other cancers can be cured using radiation therapy in combination with other treatment modalities, including breast carcinomas, rectal and anal carcinomas, locally advanced head and neck carcinomas, locally advanced lung carcinomas, advanced lymphomas, bladder carcinomas, soft tissue sarcomas, and pediatric tumors, among others [7].

Fractionation, as already mentioned, is the process of dividing up the treatment into multiple sessions, often daily across multiple weeks [8]. Typical radiation therapy treatment may include daily fractions of 1.5 to 3 Grey (Gy) of dose delivered over several weeks [7]. Data-driven analysis of fractionation has lead to greater understanding of the way cancers and tissues heal and allows for even more effective treatment.

Brachytherapy Brachytherapy is an internal radiation therapy technique where a radiation source is placed inside the body to dose the patient. In brachytherapy, radiation is delivered from an internal source. Due to the localization of the radiation, delivery is very accurate and tends to have a very steep dose falloff, allowing very precise dose delivery. However, brachytherapy is difficult to perform, and since it requires physically placing a radiation source inside the body, it works best for tumors with easier access [15].

External Beam Radiation Therapy (EBRT) External Beam Radiation therapy is the oldest and most common form of radiation therapy, where dose is delivered from an external radiation source to the tumor. In this thesis, "radiation therapy" refers to external beam radiation therapy, unless otherwise specified. In the past, Radiation therapy was delivered in two dimensions, meaning that the radiation is delivered from a single angle. This has been replaced by 3D radiation therapy based on CT imaging, which can provide dosage to the tumor from multiple angles in order to better distribute dose through the healthy tissues so that the healthy tissues can heal more quickly [7].

One key step in EBRT is fluence map optimization. Fluence map optimization seeks to

find the best angles and intensities from which to irradiate the tumor so that the actual radiation dose is as close as possible to the prescribed dose, subject to constraints that ensure that the nearby organs-at-risk (OARs) are not significantly damaged [42]. This aims to produce maximal tumor reduction with minimal damage to healthy tissues, thus reducing side effects and improving patient quality of life during treatment.

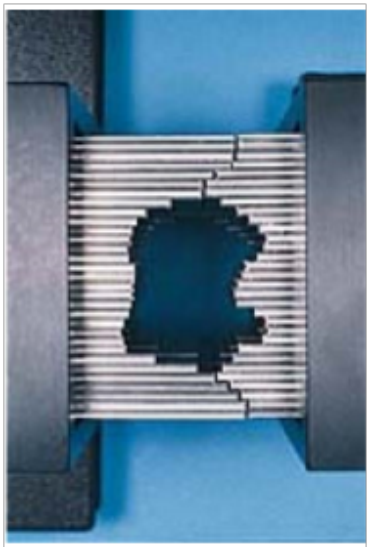

Figure 1.3: Example of a Collimator Head [18]

Intensity Modulated Radiation Therapy (IMRT) uses more sophisticated planning software and computer-controlled intensity modulation of multiple beams of radiation [7]. This allows treatment planners to create irregular dose shapes that can minimize radiation delivery to healthy tissues outside the tumor. Modern radiation therapy uses a collimator (Figure 1.3), which has metal "leaves" that can move in and out in order to fit the shape of the tumor.

While photons were the original particle used in radiation therapy, and are still the most common, other radiation sources have become more widely used in recent years. Electron beams are particularly useful for tumors close to the surface because they do not penetrate very deeply into the tissues [7]. Neutrons and protons are also used and can have benefits in different situations due to their different absorption profiles, allowing more of the dose to be delivered inside the patient without damaging the skin [7]. Furthermore, these heavier particles may be more effective at treating radio-resistant tumors [29], and they are especially useful in situations where maximal normal tissue sparing is crucial [45].

1.2 Spatially Fractionated Radiation Therapy

Spatially Fractionated Radiation Therapy (SFRT) similarly splits the dose, but in this case the dosage is split up *spatially* into different parts of the tumor, as opposed to conventional radiation therapy treatment methods, where a consistent dose of radiation is delivered across the entire tumor volume. Spatially Fractionated Radiation Therapy (SFRT) attempts to deliver a high dose of radiation to specific regions while sparing the other regions of the tumor. SFRT has gained interest in the research community in recent years as an alternative that can be used to spare healthy tissues and reduce side effects but achieve tumor reduction comparable to conventional radiation therapy, especially in large or bulky tumors, such as some of those that can be found in the abdomen and lung [30, 31, 35]

SFRT is often used to shrink the tumor before other treatment methods are used. It is similar to brachytherapy, as they both result in the deposition of spherical dosage inside the body. However, because brachytherapy deposits the radiation directly within the tumor, brachytherapy can deliver a much higher dose to the tumor, triggering necrosis. However, sometimes brachytherapy is not feasible for certain tumors, so SFRT can be implemented for similar tasks. By dispersing the radiation into spheres across the tumor, a high dose can still be delivered to the patient without causing excessive tissue damage.

1.2.1 Origins of SFRT

Grid therapy is one of the oldest SFRT techniques, with early versions using sieve-patterned collimators that administer dose in 2-dimensional beams through the entire tumor [9]. The dose deposition of Grid therapy can be seen in Figure 1.4. Lattice therapy is a more modern 3-dimensional variant that utilizes Intensity Modulated Radiation Therapy (IMRT), which offers more precise dose deposition than other radiation therapy methods, to deliver dose to small spheres inside the tumor.

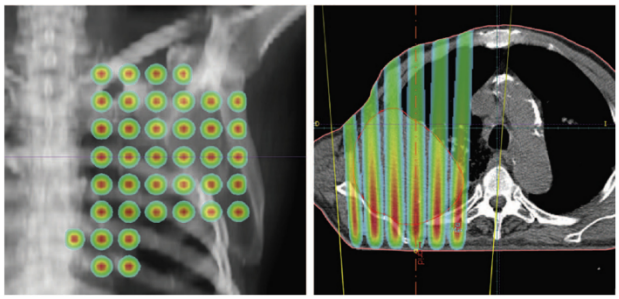

Figure 1.4: Grid therapy with a 2-dimensional dose distribution [18]

1.2.2 Treatment Planning Process

Modern clinical use of radiation therapy is heavily dependent on high quality imaging technology. Images are mostly acquired via computed tomography (CT) scans [12], but other imaging techniques can be used for different tumors (e.g., magnetic resonance imaging (MRI) [51] or positron emission tomography (PET) [43]). Once radiation therapy is prescribed, the treatment planning starts with obtaining images of the cancerous areas in the body. Once all the imaging is completed, the "delineation process" will be started [39].

Specifically, the process starts with tumor delineation, where the gross tumor volume (abbreviated as GTV in clinical domain) is identified based on the pathology results and expert's judgment. GTV is the so-called visible cancerous area. The GTV is further expanded to obtain the clinical target volume (CTV), which includes surrounding areas that are susceptible to be affected by the microscopic cancer spread. Finally, CTV is expanded to a greater volume, referred to planned clinical volume (PTV), which mainly accounts for possible movement of the tumor due to patient's breathing during radiation therapy. The process of designating these areas in the imaging (i.e., in the CT) is referred to as "contouring process."

The contouring process also involves identification of the healthy tissues and structures, that surround the PTV, which are referred to as organs-at-risk. It is crucial to identify OARs and their boundaries, because the clinician aims at maximizing the dose at PVT, while minimizing the dose that is unfavorably received by the OARs, which is the main cause of treatment toxicities and reduced quality of life in the patients. In summary, the result of the contouring process is the identification of PTV(s) and all OARs, which are collectively referred to as regions-of-interest (ROIs).

Once all ROIs are identified, the treatment planners identify the prescribed dose to be delivered to each ROI. They must determine peak dose and valley dose. Peak dose is the dose prescribed to radiation spheres and valley dose is the dose prescribed to parts of the tumor that are not targeted by a radiation sphere. Valley dose is generally 20-30% of peak dose [53]. The various ROIs can be given different weights, where deviation from the target dose is more strongly penalized for some ROIs than others. Next, the treatment planners place constraints on the dose that will be delivered to each structure in the set of ROIs. There are three main constraints commonly used in radiation therapy: max/min constraints, average dose constraints, and dose-volume histogram constraints. Maximum and minimum constraints prescribe the maximum and minimum total dose that can be delivered to any ROI within the body. Average dose constraints prescribe the maximum and minimum average dose that can be delivered to any ROI within the body.

After all of the planning is done, treatment planners use software to calculate ideal angles and intensities of radiation beams in order to irradiate the tumor while doing the least damage to nearby OARs. This process is known as fluence map optimization.

SFRT is unique because only specific parts of the tumor are irradiated with a high dose (peak dose) of radiation. High radiation dose should be localized within small spheres placed throughout the tumor, often laid out in a grid pattern. For SFRT, part of the contouring process is determining the locations of these spheres subject to treatment guidelines. The following is the key requirement prescribed in the current guidelines for SFRT Lattice Therapy [21, 52]:

> **Requirement:** Spatial placement of high radiation dose must be done through 1.5-cm diameter spheres with an ideal center-to-center distance of 3 cm.

1.3 Research Gap

Proper contouring and sphere placement is essential for consistent high-quality treatment. However, guidelines and placement techniques can vary between institutions, and even among expert treatment planners given the same guidelines, they can place vastly different numbers of spheres within the tumor. This is a gap in the current research: What is an effective and robust way to ensure consistent high quality contouring for SFRT? A robust contouring methodology that can consistently produce quality sphere placements will help experts

guarantee consistent high-quality treatment and patient outcome.

However, there is a lack of rigorous mathematical optimization in the SFRT sphere placement process. Currently, there are no guidelines that specify how spheres should be placed within a tumor. There is only one major paper by Zhang et al. that attempts to find the optimal placement of spheres. Their model takes an initial sphere placement as an input and allows the grid to shift within the tumor to find the optimal location of the entire grid [53]. This methodology is highly dependent on the initial position of the GRID, which has been shown to be inconsistent across different treatment planners. Furthermore, this technique is unable to place a different number of spheres than what is given in the initial placements. Our model will expand upon this by removing the need for an initial grid placement and allowing for any number of spheres to be placed in any orientation, giving a wider set of feasible sphere placements that will create a more flexible and robust model. More on this paper will be discussed later, as it is the only significant paper that attempts to optimize SFRT sphere placement.

Thus, the goal of our research will be to design a robust decision making framework that determines the optimal placement of radiation spheres for Spatially Fractionated Radiation Therapy.

Research Question: How do we automate and maximize the number of spheres that can be placed in the tumor respecting MIS requirements?

Research Question: How do we integrate sphere placement with fluence map optimization to find the optimal sphere placement?

Standard fluence map optimization is done with a fixed set of prescriptions, but we will expand upon the existing framework by optimizing both the fluences and the sphere placements simultaneously.

1.4 Contributions

The SFRT treatment planning placement process can be broken down into two steps: first, spheres are placed within the tumor, and second, given that sphere placement, the optimal angles and intensities at which to irradiate the spheres are chosen. After the fluences are found, we know from a radiological standpoint how the actual dose delivered will deviate from

the prescribed dose. Using this, we can define one treatment plan as better than another if it deviates less from the prescription. Thus, the best sphere placement is the one that allows for the least amount of deviation from the resultant prescription. Placing spheres manually is difficult because they must place spheres within the guidelines in three dimensions but on two dimensional planes, and this must be done while considering which organs the radiation may have to pass through in order to reach the sphere. This is a difficult two-step decision-making problem to which mathematical optimization can contribute.

The problem of sphere placement is especially complex because, despite research and long term clinical use, the exact mechanisms that make SFRT effective are still under investigation in the scientific community. It is generally understood that there are bystander effects such that tumor cells that did not receive a high dose of radiation, but are nearby cells that received a high dose will die, but the specific mechanisms that underlie this process are not fully known. However, for the purposes of treatment planning, the goal of radiation therapy in general is to maximize dosage to the tumor while minimizing dosage to the surrounding healthy tissues, thus the placement of the spheres should be done with this objective in mind.

Conventionally, SFRT places points on a consistent square grid-pattern through the tumor [21]. This results in a relatively consistent pattern of dose oscillation through the tumor. We relax this grid-pattern convention to provide a more flexible decision-making framework (Figure 1.5). We justify this relaxation by assuming that a tight grid placement, meaning one in which all spheres are close together, will result in a relatively consistent pattern of dose oscillation that is similar to that of the conventional square grid-pattern. Furthermore, since the prescription is per-voxel, a greater number of spheres will result in a greater overall dose to the tumor, which will result in more tumor reduction.

Model Assumption: Our model relaxes the convention of a square grid of spheres placed within the tumor. We assume that if a MIS is placed, the resultant radiological profile will be locally similar to that of a square grid and result in similar patient outcomes.

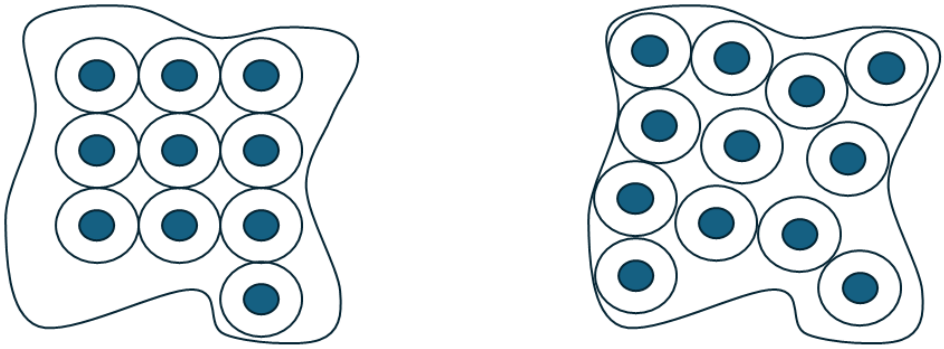

(a) Standard SFRT Placement (b) Proposed Relaxation

Figure 1.5: Conventional SFRT Sphere Placement vs the Proposed Relaxation to Sphere Placement

By maximizing the total number of spheres, the spheres will be forced to be close together, thus giving a denser, albeit more geometrically complex arrangement of spheres in 3-dimensional space, that should emulate the consistent dose variation associated with the square grid while allowing for a wider set of geometric layouts that can better fit the geometrically complex shape of the borders of the tumor.

To address this decision-making problem, this thesis will be split into two major sections. The first part will deal with the modeling of the decision making problem of how to place the maximum number of spheres within the tumor. The second part of the thesis will incorporate the quality of the optimal dose delivery based off of the sphere placements from section one in order to differentiate between multiple optimal solutions and account for treatment plans that may be better for the patient while using less spheres.

Most of the data for this paper is obtained from PortPy, which is a Python library on GitHub that provides open-source tools for research of radiation therapy. PortPy contains many useful functions for radiation therapy treatment planning, as well as a curated library of patients. PortPy contains a library of 50 lung cancer tumors curated from the National Cancer Institute Cancer Imaging Program. All of these tumors are from the NCI cancer imaging archive "NSCLC-Radiomics": https://doi.org/10.7937/K9/TCIA.2015.PF0M9REI. The optimization pipeline (Figure 1.6) will take inputs from PortPy as well as the raw CT scan. Using these, a graph will be constructed that will represent the tumor and requisite optimization parameters will be generated. Using this graph, we will place the most number of spheres that can be placed in the tumor using the maximum independent set (MIS) problem

and use this to warm-start our optimization model. Then, we will, either sequentially or in parallel, find the optimal sphere placements for various numbers of spheres, warm starting using the original MIS and removing nodes to generate a good feasible solution. After all models have finished or the time limit is up, the model will return optimal sphere placements for multiple numbers of spheres, as well as the dose deposition and dose deviation to all ROIs, as well as the beamlet intensities that created the resultant dose deposition.

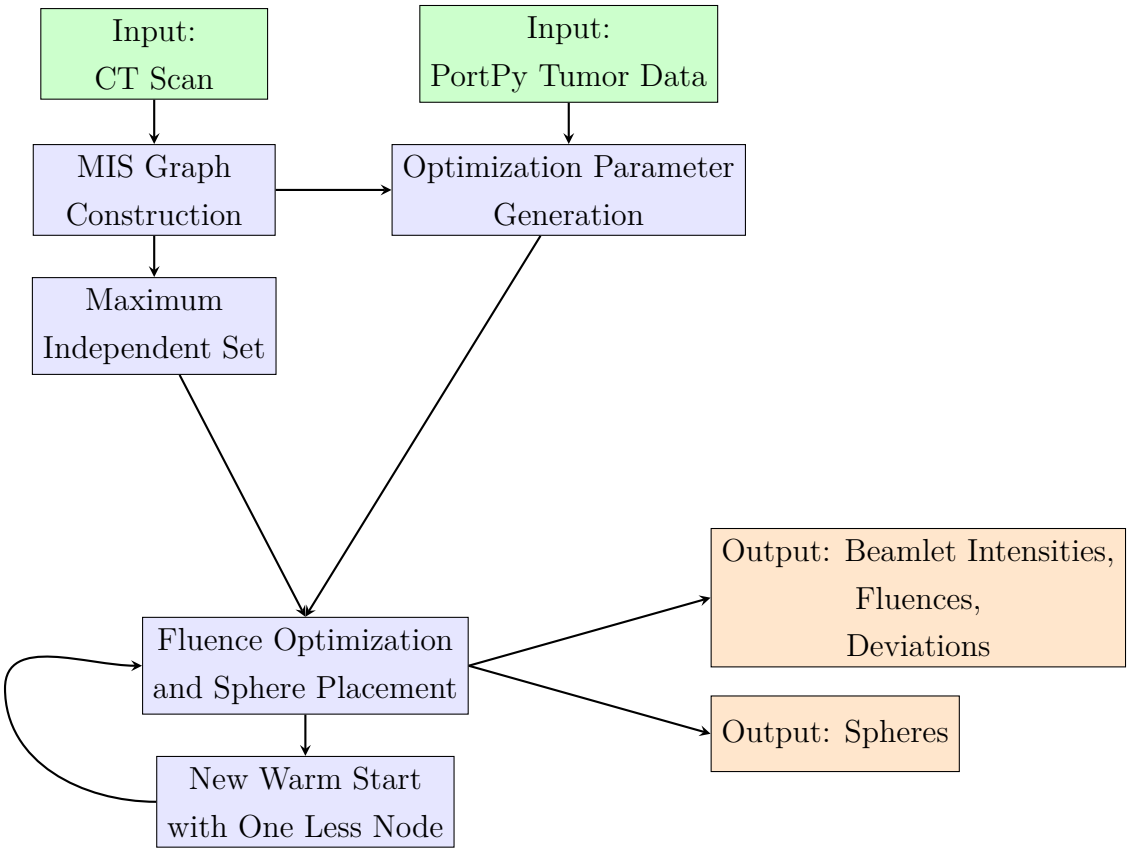

Figure 1.6: Proposed Optimization Pipeline

Chapter 2

The SFRT Contouring Problem

In this chapter, we will address the following key question in the contouring task of SFRT:

> **Key question:** Given the geometry of a tumor, possibly in irregular shape, what is the number of maximum spheres that can be placed within the tumor, while ensuring the main requirement (see Section 1.3) is met?

To answer this question, we need to represent a tumor's geometry and formulate a mathematical model that can compute the maximum number of spheres that can be placed within the tumor while respecting the requirements of SFRT contouring process. The remainder of this chapter is as follows. We will discuss some preliminaries in Section 2.1, which is relevant to graph representation of our the problem. In Section 2.2, we present our method to represent the geometry of the tumor. Section 2.3 discusses several formulations, based on the so-called maximum independent set (MIS) problem, for the placement of spheres. We will present the result of the proposed MIS model in Section 2.4 and provide some discussions in Section 2.5. We will provide some concluding remarks in Section 2.6. For the sake of easier reading, Table 3.1 provides all the notations used in this chapter.

2.1 Preliminaries

Let $G(N, E)$ be a graph with N and E being the set of nodes and the set of (undirected) edges, respectively. Given $G(N, E)$, an *independent set* of nodes is a subset $S \subseteq N$ such that

Table 2.1: Table of Notations for Chapter 2

Notation	Type	Description
G	Graph	A discretized structure with nodes and edges or arcs.
N	Set	Set of nodes, indexed by i
E	Set	Set of undirected edges, indexed by $\{i, j\}$
$\mathcal{N}_i$	Set	Set of nodes adjacent to i
x_i	Decision Variable	Binary selection of candidate sphere i
A_D	Parameter	Adjacency Matrix
I	Parameter	Identity Matrix

no two nodes in S are connected by an edge [11], i.e., for each pair of nodes $i, j \in S$, we must have $\{i, j\} \notin E$. Note that we have used the notation $\{i, j\}$ (instead of $(i, j) \in E$) to refer to the edge connecting nodes $i, j \in N$ because we assume G is undirected. Figure 2.1 shows a sample graph (Figure 2.1a) along with an independent set (Figure 2.1b) as well as two alternate maximum independent sets (Figure 2.1c, 2.1d).

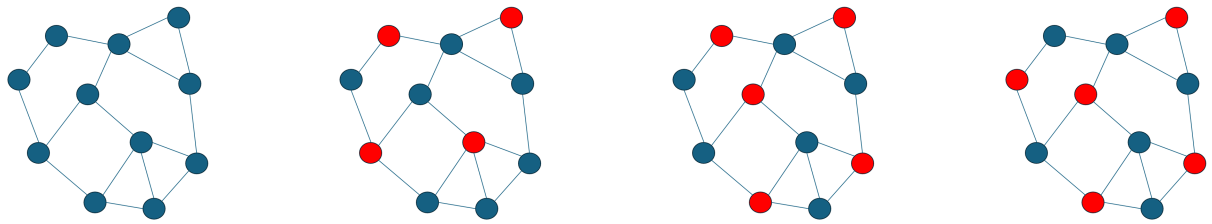

(a) (b) (c) (d)

Figure 2.1: The Maximum Independent Set

The problem of finding the Maximum Independent Set (MIS) of a graph is NP-hard. The notion of NP-hardness (and the closely relevant notion of NP-complete) is a fundamental concept in theoretical computer science. Informally, it suggests that it is unlikely that an efficient algorithm exists for finding the MIS of a given graph. More rigorously, this indicates that the computational effort required to find the MIS of a given graph grows exponentially as the size of the graph increases (e.g., as the number of nodes and edges increases). Proving this result requires the construction of a rigorous mapping (formally, reduction) that transforms any instance of an existing NP-complete problem to an instance of MIS. For MIS, a relevant NP-complete problem is the maximum clique problem, which is one of the well-known NP-complete problems in Karp's 21 NP-complete problems [25]. To define the maximum clique problem, consider any graph $G(N, E)$ and define a subgraph of G as a graph $G'(N', E')$ with $N' \subset N$ and $E' \subset E$. A clique of a graph G is then a subgraph G' with an

additional constraint that given $i, j \in N'$, there exists an edge $\{i, j\} \in E'$. Such a subgraph is referred to as a *complete* graph. The maximum clique problem then seeks, given $G(N, E)$, a complete subgraph of G that has the maximum number of nodes. Interestingly, MIS and the maximum clique problem are complementary, in the sense that finding the maximum clique of a graph $G(N, E)$ reduces to a combinatorial problem in which one must find any MIS within the graph $G(N, \bar{E})$, where $\bar{E} = \{\{i, j\} : i, j \in N,\ \{i, j\} \notin E\}$.

The MIS problem has been studied for over 50 years, and many algorithms have been developed to solve the problem efficiently. Through computational experimentation, the MIS problem has been shown to have an effective integer programming implementation in Gurobi [5, 32, 44, 49]. Our empirical results show that Gurobi's MIS implementation is fast enough to provide quality results in under 10 minutes for all tumors that are not excessively large. This will be expanded upon in the results section of this chapter.

Our motivation to study the MIS model originates from the fact that it can accurately represent the grid placement problem in SFRT where the goal is to maximize the number of spheres to be placed in the tumor (i.e., PTV). More specifically, we will devise an algorithm that converts the **continuous and possibly irregular** geometry of the tumor into a discretized structure represented by a graph. In this graph, each node will represent a candidate location for placing the spheres, and an edge between any two nodes indicates that simultaneous placement of spheres at those locations is prohibited due to their violation of SFRT spacing constraints (see Section 1.3).

2.2 Graph Construction

2.2.1 Tumor Discretization

The first task is to find all the feasible centers of radiation spheres. The tumor boundary is geometrically complex, so the first difficulty lies in determining whether a given point is within the tumor or not. To this end, we draw from a well-known principle in computational geometry called Ray-Casting [22, 54]. Ray-Casting algorithms rely on the property that for a closed three dimensional shape, any ray that emanates from the exterior of the shape and crossed the boundary of the shape an odd number of times ends inside the shape [24]. This

works in two dimensions as well, as long as every component sits within the plane.

The general problem is known as the point-in-polygon problem, which determines whether or not a given point lies within a polygon. Ray-Casting Algorithms, crossing-rule algorithms, and the even-odd rule algorithm all essentially determine whether or not a point is within a shape [20, 24]. They are often used in volume rendering [22, 54]. These algorithms come in multiple forms for various levels of generalization, the simplest form creates a line segment from the point to a point guaranteed to be outside of the polygon. Our algorithm adopts the methodology of these existing algorithms for our purposes.

Using this property, our algorithm creates rays (called x-lines) that emanate from the outside of the tumor. The algorithm finds the points where each ray (x-line) crosses the tumor boundary by creating a linear approximation of the tumor border. The algorithm must also find all points of tangency, where a ray touches the tumor boundary but does not cross it. These points are added to the set of candidate spheres and removed from the algorithm, since they do not correspond to an actual entry or exit.

The quality of the discretization is a function of its granularity. A higher granularity will provide a better solution resolution, but will increase the size of the model substantially. Thus, it is very important to determine a quality discretization granularity. A 1 cm grid granularity was chosen for each slice that sits 2.5 mm apart from the adjacent slices. However, a 1 cm grid is large enough to restrict the number of options from which the mathematical model can select from. Thus, multiple discretization methods will be examined in order to ensure solution quality.

Model Assumption/Limitation: Spheres can only be centered at discrete points within the tumor. We assume that our $1 \times 1 \times .25$ cm granularity is fine enough to properly represent all feasible positions that a sphere should be able to sit within the tumor.

2.2.2 Algorithms

The following algorithms take a CT scan and a predetermined grid granularity g as inputs and finds all points inside the tumor volume (Figure 2.2). These points correspond to the centers of every feasible candidate sphere.

CT-scans are stacks of two dimensional images. The imaging machine extracts cross-sectional slices (z-slices) that are stacked on top of each other to produce a composite view of the entire tumor. For our data, CT-scan slices are 2.5 mm apart. During the contouring process, the treatment planner uses software to draw lines that define the shape of the tumor. The tumor border for each slice is stored in the form of border points, which are (x, y) points for each z-slice, which define the boundary of each ROI. These points are ordered in a list. These points, as well as the desired granularity g, are the only inputs into this algorithm.

Let $p_1,\ p_2,\ ...,\ p_Q$ be the (arbitrarily) ordered list of all input border points for the perimeter of the ROI on slice z. Define $\mathcal{Q}_k$ as the set of all q indices of the points p. There can be multiple sets of border points for a given z, which would signify a hole or gap, these sets K are indexed by k. We will denote $\bar{x}_q$ and $\bar{y}_q$ as the coordinates of $p_q,\ q \in \mathcal{Q}_k$, represented in millimeters. All indexes start at 1. Further, define X to be the list of all x-lines, and $\mathcal{I}$ to be the list of all indices of X. Thus, the set of x-lines is $\{x_i\ \forall\ i \in \mathcal{I}\}$. Similarly, the set of all y values of a border crossing on an x-line, corresponding to $x_i,\ i \in \mathcal{I}$, is Y_i, with the set of indices $\mathcal{J}_i \coloneqq 1, 2, ..., J_i$, indexed by $j \in \mathcal{J}_i$. Finally, define the function $f_{p_q,p_{q+1}}(x_i)$ to be the liner interpolation function between two border points p_q and p_{q+1}. The function f_{p_i,p_j} is the line between point p_i and $p_j,\ \forall\ i, j \in \mathcal{Q}_k,\ k \in K$. $f_{p_i,p_j}(x_i)$ is the value of the line f_{p_i,p_j} at x_i. Note the convention that $f_{Q,Q+1}(x_i)$ is the linear interpolation of x_i between P_Q and P_1.

For each slice $z \in Z$, Algorithm 1 finds the bounds of the tumor in the x direction, creating a list X, which is the list of all feasible x values (x-lines) within the tumor at the given granularity. All rays exist on x-lines.

The algorithm determines the border of the shape by linearly interpolating between adjacent border points. If an x-line is between two adjacent border points, the x-line must cross the tumor boundary at some point between these two adjacent border points. Thus, the linear interpolation between the two border points at the x-line is found and counted as a border crossing.

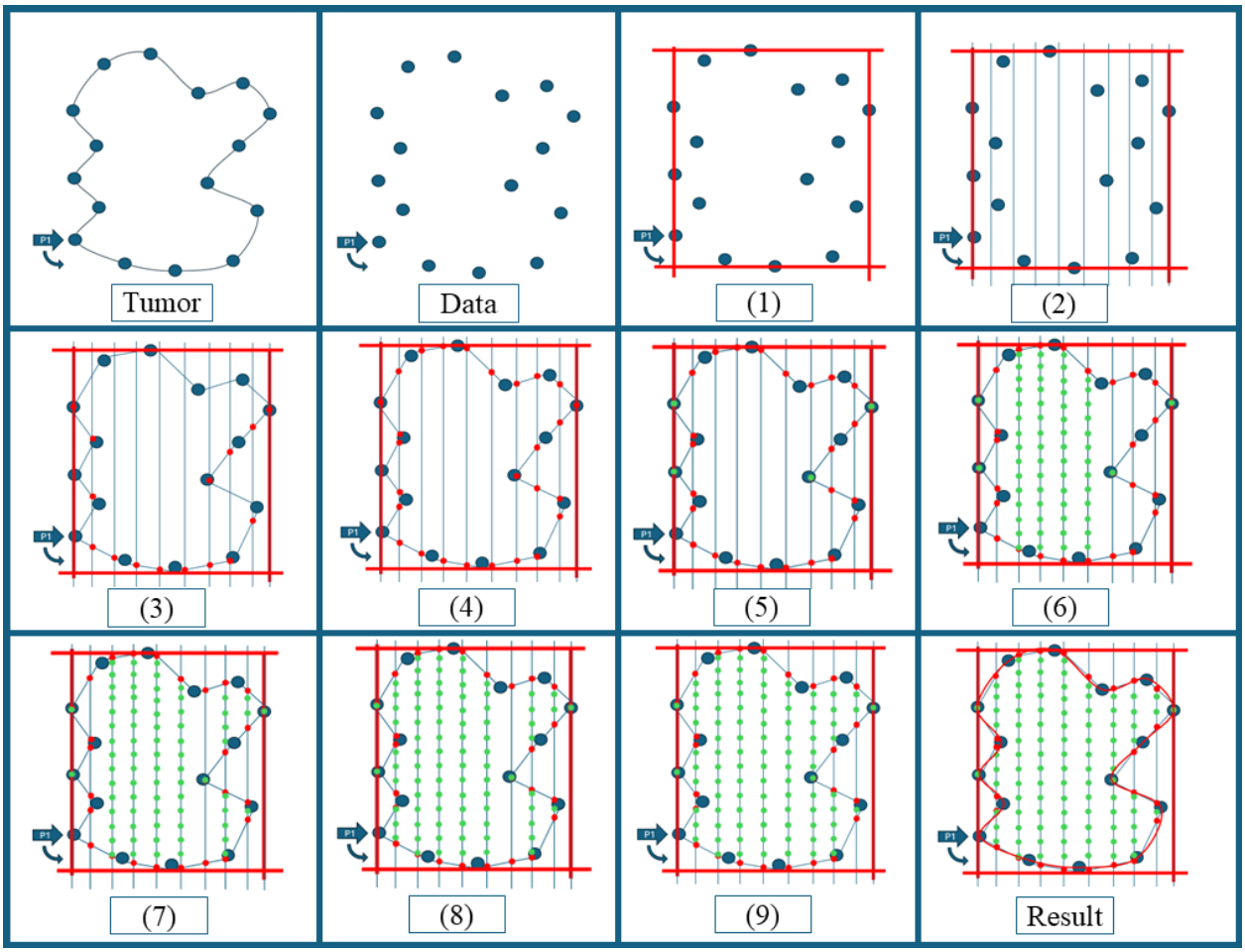

Figure 2.2: An example of a CT slice being discretized. (Starting top left) The actual shape of the original tumor; The actual data obtained form the CT scan: a list of coordinates; (1) obtain tumor bounds; (2) discretize in the X-axis; (3) Use linear interpolation to find where each x-line intersects the tumor border, where $\bar{x}_q \leq x_i < \bar{x}_{q+1}$ (4) Same as panel 3 but for the "top" of the tumor, where $\bar{x}_{q+1} \leq x_i < \bar{x}_q$; (5) Placing points on x-lines with 2 corresponding y values; (6) Placing tangent points; (7) Placing points on x-lines with an even number of y values greater than 2; (8-9) Placing points on x-lines with a tangency and a tumor section; Resulting discretization showing linear approximation (blue) vs the actual tumor boundary (red)

Lines 13-19 find any points where the tumor is tangential to the x-line, and does not cross the tumor boundary. Since the tumor is approximated with straight lines, the only way a tangency can exist is if the tangent point is also within the set of border points that define the shape of the tumor. This is a necessary, but not sufficient condition to determine tangency. Since the tangent point is centered at a border point, the two border points adjacent to the tangent point must be on one side of the tumor. When this tangent point is found, it is added as a candidate point and removed from the list of border crossings.

The algorithm is robust to edge cases. This algorithm works if an entire line of the tumor border is tangent to an x-line. This would mean that these share a line segment. Since lines 13-19 only remove points if the adjacent border points are on the same side of the tangent point (evaluated with an inclusive range), the algorithm will place points along this tangent line.

This algorithm also works if the tumor is not continuous. Because this algorithm discretizes slices, a nonconvex tumor can have disjoint slices. However, all sections of the tumor that appear on a slice will be closed, and the algorithm will operate normally, because it can accommodate any number of border crossings. Each x-line is dealt with independently, so the algorithm is oblivious of any hole or division in the tumor shape.

Algorithm 1: Candidate Point Algorithm

Algorithm 2 takes the entire CT scan and calls Algorithm 1 on each z-slice, which finds the list of all candidate sphere centers (or "Nodes") N. It then calculates the distance between each pair of nodes and creates an edge between any two nodes that are too close together to coexist, with a distance less than η. For our case, $\eta = 3$ cm, in accordance with treatment guidelines [21, 53]. Thus, Algorithm 2 returns the final graph G. The MIS of G corresponds to the centers of the most number of spheres that can be placed within the tumor.

Crucially, Algorithm 1 finds all nodes that sit within the shape of the tumor, including points very close to the border. In the SFRT guidelines, each sphere must be completely within the PTV (planning tumor volume). Since each of the spheres are 1.5 cm in diameter, the center of a sphere must sit 0.75 cm from the border. However, using modern treatment planning, this is easily achieved in the contouring process by identifying a "SFRT_PTV" ROI in the CT scan, which our code can identify and use with Algorithm 1. However, since the software is not granular enough to accommodate two decimal points, we approximate it by shrinking the PTV by 0.8 cm, which is the closest graduation.

Thus, with Algorithm 1 and 2 we are able to build a graph consisting of a set of nodes, where each node is at the center of a feasible radiation sphere, and a set of edges that connect any pair of nodes that are too close together to contain a radiation sphere. This graph is a valid input for the maximum independent set problem, where the resultant MIS will be the set of nodes corresponding to the greatest number of spheres that can be placed within the tumor.

Algorithm 1 Candidate Point Extraction from Single CT Slice

Input: One CT-scan slice: (z), Grid granularity: (g)
Output: Set of candidate points: (N)

Define sets $\mathcal{J} \coloneqq \{\},\ N \coloneqq \{\},\ Y_i \coloneqq \{\},\ i \in \mathcal{I}$.
$x^{max} \coloneqq \max\{\bar{x}_q \mid q \in \mathcal{Q}_k,\ \ k \in K\}$
$x^{min} \coloneqq \min\{\bar{x}_q \mid q \in \mathcal{Q}_k,\ \ k \in K\}$
Let $X \coloneqq \{x^{min}, x^{min} + g, x^{min} + 2g,\ \ldots\ , x^{max}\}$
for $i \in \mathcal{I}$ **do**
    for $q \in \mathcal{Q}_k,\ k \in K$ **do**
        if $x_i \in [\bar{x}_q, \bar{x}_{q+1})$ **Or** $x_i \in (\bar{x}_{q+1}, \bar{x}_q]$ **then**
            $\mathcal{J} \leftarrow \mathcal{J} \cup \{J_i + 1\}$
            $Y_i \leftarrow Y_i \cup \{y_{iJ} \mid y_{iJ} \leftarrow f_{q,q+1}(x_i)\}$
        end if
    end for
end for
for $i \in \mathcal{I}$ **do**
    if $(x_i, y_{ij}) = (\bar{x}_q, \bar{y}_q)$ for any $j \in \mathcal{J}_i,\ q \in \mathcal{Q}_k,\ k \in K$ **then**
        if $\bar{x}_q \notin (\bar{x}_{q-1}, \bar{x}_{q+1})$ **And** $\bar{x}_q \notin (\bar{x}_{q+1}, \bar{x}_{q-1})$ **then**
            $N \leftarrow N \cup \{(x_i, y_{ij}, z)\}$
            $Y_i \leftarrow Y_i \backslash \{y_{ij}\}$
        end if
    end if
    $Y_i \leftarrow \texttt{Sorted}(Y_i)$ in ascending order
    for $j \in \mathcal{J}_i$ **do**
        if j is odd **then**
            $y^{min} \leftarrow y_{ij}$
            $y^{max} \leftarrow y_{ij+1}$
            $N \leftarrow N\ \cup\ \{(x_i, y, z)\}$ for each $y \in \{y^{min},\ y^{min} + g,\ y^{min} + 2g,\ \ldots, y^{max}\}$
        end if
    end for
end for
return: N

Algorithm 2 Construct Graph for Tumor Sphere Placement

Input: Set of CT scan slices: (Z), Minimum distance between points: (η)
Output: Graph: $G(N, E)$ where MIS(G) gives maximal non-overlapping spheres within the tumor

```
N ← {}                                          ▷ Initialize set of candidate points
E ← {}                                          ▷ Initialize set of graph edges
for z ∈ Z do
    N^z ← GetCandidates(z)                      ▷ e.g., from Algorithm 1
    N ← N ∩ N^z
end for
for i ∈ N do
    for j ∈ N do
        if i ≠ j and ‖i − j‖_2 ≤ η then
            E ← E ∪ {(i, j)}
        end if
    end for
end for
return G(N, E)
```

2.3 MIS Formulations

We will explore three formulations of the MIS problem: the arc-based method, the node-based method, and a quadratic nonlinear method.

2.3.1 Arc-Based Formulation

The first implementation takes a set of nodes N and a set of edges E and introduces a binary decision variable $x_i \; \forall \; i \in N$, where $x_i = 1$ if node i is in the MIS, and $x_i = 0$, otherwise. The formulation is as follows (Model 2.1).

$$\max \quad \sum_{i \in N} x_i \tag{2.1a}$$

$$x_i + x_j \leq 1 \quad \forall (i, j) \in E \tag{2.1b}$$

$$x_i \in \{0, 1\} \tag{2.1c}$$

$$\tag{2.1d}$$

As shown in Figure 2.3, this model maximizes the number of nodes in the MIS while

ensuring that no two adjacent nodes are both selected.

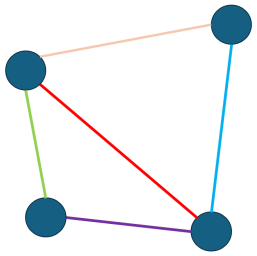

(a) Arc-Based Formulation: Each arc has a unique constraint

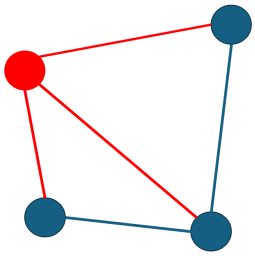

(b) Node-Based Formulation: Each node has a unique constraint

Figure 2.3: Arc and Node Formulations

2.3.2 Node-Based Formulation:

The node-based model uses the same variables but introduces the set $\mathcal{N}_i$ which is the set of nodes adjacent to node i, and is defined for each node $i \in N$ (Equations 2.2).

$$\max \quad \sum_{i=1}^{N} x_i \tag{2.2a}$$

$$\text{s.t.} \quad x_i + \frac{\sum_{j \in \mathcal{N}_i} x_j}{|\mathcal{N}_i|} \leq 1 \quad \forall i \in N \tag{2.2b}$$

$$x_i \in \{0, 1\} \quad \forall i \in N \tag{2.2c}$$

As shown in Figure 2.3b, the node-based model ensures that if a node i is selected, no node adjacent to i can be selected.

2.3.3 Quadratic Nonlinear Model

The final formulation is the quadratic nonlinear model. This model uses the adjacency matrix A_D, which is a $|N| \times |N|$ matrix where the value of element (i, j) is 1 if nodes i and j are adjacent, and 0 otherwise. A node is not considered to be adjacent to itself in this implementation. The model employs a *shifted adjacency matrix*, $I - A_D$, which contains ones on the diagonal and negative ones in positions corresponding to entries where nodes i and j are adjacent. Then, binary quadratic optimization model 2.3 is solved.

$$\max \quad x^T(I - A_D)x \tag{2.3a}$$

$$x_i \in \{0, 1\} \quad \forall i \in N \tag{2.3b}$$

In this implementation, if any pair of nodes are selected, the contribution to the objective function will be -1, thus these solutions will not be selected. However, the model is still incentivised to select the most nodes, since all diagonal entries of the A matrix are ones.

2.4 Explanation of Data

We use the CT scans provided by the NCI, and curated by PortPy as data points. From these 50 tumors, we identify 8 variously sized tumors with a PTV volume greater than 300 cm^3 that are good candidates for SFRT (Table 2.2, Figure 2.4). Five of these are used for MIS experimentation.

Patient ID	**PortPy Patient ID**	**NCI CT ID**	**PTV Volume (cm^3)**
1	4	5	312.6
2	22	34	348.3
3	14	22	357.2
4	17	25	372.6
5	25	42	476.3
6	21	33	662.6
7	24	40	733.2
8	15	23	1276.9

Table 2.2: Patient Metadata

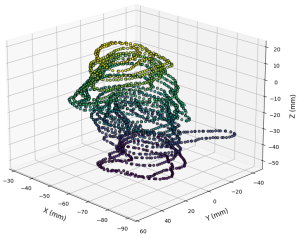

Tumor 1

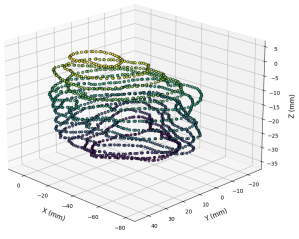

Tumor 2

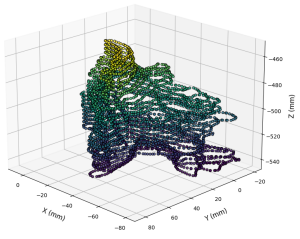

Tumor 6

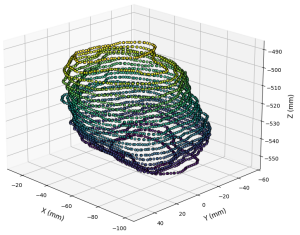

Tumor 7

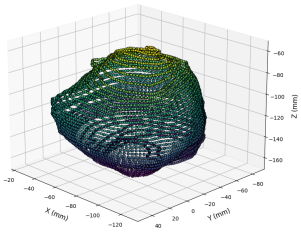

Tumor 8

Figure 2.4: PTV Visualization for MIS Experimental Data

2.5 Discretization Experiments

The greatest concern with our proposed approach is the discretization. By discretizing the tumor into feasible candidate sphere positions, we are restricting the number of places that a sphere can be. If the tumor is very complex and the discretization is very course, nuances of the tumor shape could be missed, whereas a finer resolution can better represent the complex nuance of the tumor border. Notably, the slices are only 2.5 mm apart, so there is a higher granularity in the z-plane. This complexity improves the solution quality, but we still investigate multiple tumor grid discretization techniques in order to evaluate discretization quality.

2.5.1 Setup

We investigate two different discretization factors: grid shape and slice independence. The grid can come in two different shapes, square and triangular. The square discretization is the same as is shown in algorithm 1, but the triangular discretization creates equilateral triangles with 1 cm sides. with an initial granularity of g, This is done by changing the distance between each x-line to $\sqrt{g^2 + (\frac{g}{2})^2}$, and offsetting every other y-ray by $0.5g$

(a) Square discretization

(b) Triangular discretization

Figure 2.5: Square vs Triangular Grid

Slice independence comes in two forms: Fixed and Relative. In Algorithm 1 and 2, the grid on each z-slice is dependent on the shape of the tumor. This allows each grid to be offset from the others within the tumor. Fixed discretization starts the algorithm with a universal set of x and y tumor max and min bounds, across all z-planes. This ensures that each candidate grid is directly above the one below it.

(a) Relative Discretization

(b) Fixed discretization

Figure 2.6: Fixed vs Relative Discretization

By crossing these two experimental axes, we can see that there are 4 total experiments

to be done. Five various sized tumors from the PortPy library were chosen and used for experimentation. All MIS formulations were ran for every discretization technique. This give a total of 60 experiments.

2.5.2 Experimental Results

Results of these experiments are shown below (Table 2.3). Experiments were ran for 10 minutes, and the optimality gap at that time was recorded.

Table 2.3: Summary of MIS Optimization Results

Patient	Grid	Slices	Formulation	Nodes	Edges	MIS	Gap (%)	Time (s)
1	Square	Fixed	Arc	273	33296	10	0	0.708
1	Square	Fixed	Node	273	33296	10	0	1.727
1	Square	Fixed	Non-Linear	273	33296	10	Inf	600
1	**Square**	**Relative**	**Arc**	**326**	**44934**	**13**	**0**	**2.085**
1	Square	Relative	Node	326	44934	13	0	6.008
1	Square	Relative	Non-Linear	326	44934	13	Inf	600
1	Triangle	Fixed	Arc	327	47464	11	0	2.323
1	Triangle	Fixed	Node	327	47464	11	0	4.965
1	Triangle	Fixed	Non-Linear	327	47464	11	Inf	600
1	Triangle	Relative	Arc	352	53362	12	0	2.766
1	Triangle	Relative	Node	352	53362	12	0	6.051
1	Triangle	Relative	Non-Linear	352	53362	12	Inf	600
2	Square	Fixed	Arc	264	31362	9	0	1.055
2	Square	Fixed	Node	264	31362	9	0	3.148
2	Square	Fixed	Non-Linear	264	31362	9	Inf[1]	60
2	Square	Relative	Arc	314	42536	9	0	0.394287
2	Square	Relative	Node	314	42536	9	0	1.394877
2	Square	Relative	Non-Linear	314	42536	9	Inf	600
2	Triangle	Fixed	Arc	308	44384	8	0	0.3704
2	Triangle	Fixed	Node	308	44384	8	0	1.3582
2	Triangle	Fixed	Non-Linear	308	44384	8	Inf	600
2	**Triangle**	**Relative**	**Arc**	**344**	**52360**	**10**	**0**	**0.48338**
2	Triangle	Relative	Node	344	52360	10	0	1.93192

Continued on next page

[1]The notation Inf indicates that the gap is very large.

Patient	Grid	Slices	Formulation	Nodes	Edges	MIS	Gap (%)	Time (s)
2	Triangle	Relative	Non-Linear	344	52360	10	Inf	600
6	Square	Fixed	Arc	538	81206	17	0	1.21
6	Square	Fixed	Node	538	81206	17	0	3.8675
6	Square	Fixed	Non-Linear	538	81206	17	Inf	600
6	**Square**	**Relative**	**Arc**	**644**	**105784**	**20**	**0**	**1.9661**
6	Square	Relative	Node	644	105784	20	0	6.5651
6	Square	Relative	Non-Linear	644	105784	20	Inf	600
6	Triangle	Fixed	Arc	606	106684	17	0	2.5738
6	Triangle	Fixed	Node	606	106684	17	0	9.801
6	Triangle	Fixed	Non-Linear	606	106684	17	Inf	600
6	Triangle	Relative	Arc	667	121178	19	0	2.308
6	Triangle	Relative	Node	667	121178	19	0	6.76323
6	Triangle	Relative	Non-Linear	667	121178	19	Inf	600
7	**Square**	**Fixed**	**Arc**	**908**	**186436**	**21**	**0**	**10.12536**
7	Square	Fixed	Node	908	186436	21	0	83.97335
7	Square	Fixed	Non-Linear	908	186436	20	785	600
7	Square	Relative	Arc	990	212466	21	0	75.70451
7	Square	Relative	Node	990	212466	21	4.761	600
7	Square	Relative	Non-Linear	990	212466	21	633.3333	600
7	Triangle	Fixed	Arc	1052	260506	20	0	25.07724
7	Triangle	Fixed	Node	1052	260506	20	5	600
7	Triangle	Fixed	Non-Linear	1052	260506	20	865	600
7	**Triangle**	**Relative**	**Arc**	**1096**	**274118**	**21**	**0**	**93.1648**
7	Triangle	Relative	Node	1096	274118	21	4.7619	600
7	Triangle	Relative	Non-Linear	1096	274118	20	855	600
8	**Square**	**Fixed**	**Arc**	**2213**	**544092**	**42**	**11.904**	**600**
8	Square	Fixed	Node	2213	544092	41	17.07	600
8	Square	Fixed	Non-Linear	2213	544092	41	Inf	600
8	Square	Relative	Arc	2316	594074	41	21.9	600
8	Square	Relative	Node	2316	594074	40	32.5	600
8	Square	Relative	Non-Linear	2316	594074	40	Inf	600
8	Triangle	Fixed	Arc	2541	756730	40	25	600
8	Triangle	Fixed	Node	2541	756730	39	33.3333	600
8	Triangle	Fixed	Non-Linear	2541	756730	40	Inf	600
8	Triangle	Relative	Arc	2623	778536	41	21.9512	600
8	Triangle	Relative	Node	2623	778536	40	30	600

Continued on next page

Patient	Grid	Slices	Formulation	Nodes	Edges	MIS	Gap (%)	Time (s)
8	Triangle	Relative	Non-Linear	2623	778536	40	Inf	600

2.5.3 Discussion

The Arc formulation outperformed the other MIS implementations. The nonlinear implementation was by far the worst. The modified adjacency matrix in the quadratic optimization is not positive semi-definite, so the problem is not convex and very difficult to solve quickly.

The node-based implementation reaches a good gap in a reasonable amount of time. In one case for a large tumor, it came to the largest possible solution faster than the arc-based implementation, but the optimality gap was larger than that of the arc-based implementation.

This makes sense, as the arc-based implementation has more constraints, which should result in an LP relaxation that is tighter to the convex hull, which likely results in a lower gap.

While the arc-based formulation is better than the other formulations, the discretization methods are less clearly dominant. No single discretization technique stands out as clearly better. Oftentimes the triangular discretization results in a larger graph, but the MIS may still be larger, as in the case of patient 15. Sometimes, the results are more ambiguous. In the case of patient 24, two discretization techniques find the same MIS size. One technique is much faster than the other, but the other has a much larger graph. In the absence of strong theoretical results, we decided to use the fixed discretization with a square grid. This is because the software better accommodates this type of discretization. We can begin the discretization at a round number, which allows the result to be highly reproducible and easy to implement.

2.6 Next Steps

We have shown that we can accurately represent the tumor and place the maximum number of radiation spheres within the tumor using the above algorithms and implementations of the MIS problem. However, we have no way of knowing whether or not the plan resulting from this sphere placement will result in good patient outcomes. Currently, the only way to determine the quality of a sphere placement would be to take the result of this algorithm and run it through the treatment planning software, which can take hours, to determine the dose that would be administered to the tumor and healthy tissues. Furthermore, since the MIS problem is an integer program and thus only has integer solutions, it is very possible that there are identical solutions that our algorithm cannot distinguish between. One MIS may be better than another MIS in fluence optimization, and this disparity should be accounted for. Thus, in the next section, we plan to integrate this decision-making program with fluence map optimization. This will allow us to differentiate between various sphere placements by the damage that they will do to healthy tissues in order to find the treatment plan that maximizes damage to the tumor while minimizing damage to healthy tissues.

Chapter 3

Fluence Map Optimization

In this chapter, we expand upon the previous MIS model by accounting for treatment plan deliverability. In the previous chapter we determined how to place radiation spheres within the tumor, but the MIS model has no way of knowing how accurately the resultant treatment plan can be delivered, and it has no way of knowing how much damage will be done to healthy tissues.

Thus, in this chapter, we propose a new model that incorporates our MIS based model with fluence map optimization in order to choose the best placement of spheres that maximizes dose delivered to the tumor while minimizes dose delivered to healthy tissues.

3.1 Preliminaries

Fluence map optimization changes the angles and intensities of radiation delivery in order to minimize the deviation from the prescribed dose subject to the prescribed dose constraints [42]. The body is discretized into a set of voxels V (pixels with volume: Figure 3.1). Each voxel sits within one or more structures (or regions of interest (ROIs)). Let the set of structures be S, indexed by s. This set of all voxels within a structure is V^s for each structure s.

When the dose is delivered, the collimator head (Fig 1.3) is positioned over the target at a specific angle and the aperture is opened so that the tumor receives the prescribed dose from that angle. This single dosage of radiation from a specific angle is known as a beam. The machine will then be repositioned to a new angle and a new beam will deposit radiation.

Table 3.1: Table of Notations for Chapter 3

Notation	Type	Description
V	Set	Set of Voxels, indexed by v
B	Set	Set of Beamlets, indexed by b
S	Set	Set of Structures, indexed by s
V^s	Set	Set of Voxels in structure s, indexed by v
$\mathcal{A}^s$	Set	Set of DVH constraints in s, corresponding to α
N	Set	Set of Candidate Sphere Centers, indexed by i
E	Set	Set of Edges
A	Parameter	Dose Deposition Matrix with elements a_{vb}
C	Parameter	Target Dose Matrix for conventional RT with elements c_v
D	Parameter	Proportionality Matrix for SFRT
$\bar{D}$	Parameter	Valley Dose/OAR prescription matrix
ρ	Parameter	ρ = Peak dose - Valley dose
ϕ	Parameter	Minimum number of spheres
U^s_{max}	Parameter	Max Dose Limit for structure s
L^s_{min}	Parameter	Min Dose Limit for structure s
U^s_{mean}	Parameter	Upper Mean Dose Limit for structure s
L^s_{mean}	Parameter	Lower Mean Dose Limit for structure s
$U^{\alpha,s}_{dvh}$	Parameter	Upper DVH Limit for structure s at level α
$L^{\alpha,s}_{dvh}$	Parameter	Min Dose Limit for structure s at level α
y_b	Decision Variable	Intensity of beamlet b
x_i	Decision Variable	Selection of sphere i
z_v	Decision Variable	Dummy Variable for Linearization
$\bar{\zeta}^{\alpha,s}$	Decision Variable	Dummy variable for upper DVH constraint
$\zeta^{\alpha,s}$	Decision Variable	Dummy variable for lower DVH constraint
$\bar{\tau}_v$	Decision Variable	Dummy variable for upper DVH constraint
τ_v	Decision Variable	Dummy variable for lower DVH constraint

This process will be repeated for all beams that are prescribed. Each beam is discretized into a set of beamlets B, indexed by b that corresponds to every possible position that the patient can be irradiated from (Figure 3.1).

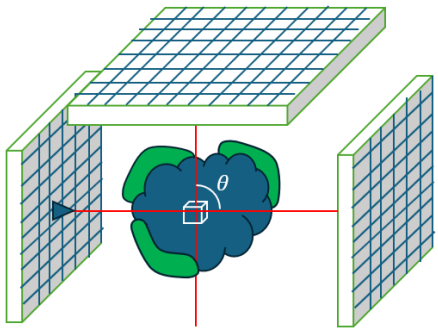

Figure 3.1: Visualization of three beams: above, left, and right, as well as the discretization of the beams into beamlets, and the deposition of two beamlets from different beams into the same voxel

Each square unit of surface area on the collimator head is a unique beamlet that can be fired independent of the other beamlets within the beam. Our model will not differentiate between various beams, so the set of all beamlets B includes beamlets from all beams. Additional constraints can also be added that place a limit on the total number of beams in order to limit treatment session duration and reduce patient discomfort. This is easily implemented by defining the set of beamlets within each beam and introducing artificial variables that limit the total number of beams used (However, this adds integer variables to what is currently a linear program). Our model accounts for this in the preprocessing stage. Treatment planners should not input all feasible beams into this model, as this will result in an extremely large model. At this stage, we rely on a treatment planner that curates a set of beams that are likely to be relevant to the treatment.

The primary decision in fluence map optimization is the intensity of each beamlet, denoted y_b for each beamlet b. Each beamlet, when fired, will deliver dose to many voxels within the body.

Romijn et al wrote one of the seminal papers in fluence optimization, which describes a linear program that implements fluence optimization [42]. The sets, parameters, decision variables, and model for conventional fluence map optimization are presented below.

3.1.1 Conventional Fluence Map Optimization Model

The goal of fluence optimization is to minimize the difference between the delivered dose and the prescribed dose. We define the prescribed dose using the $|V|$ dimensional column vector C, where element c_v is the prescribed dose to voxel v. To measure the dose delivered to each voxel, we use the matrix A, known as the dose deposition matrix. The dose deposition matrix is a $|V| \times |B|$ dimensional matrix with entries a_{vb}. The value of each element a_{vb} is the dose deposition to voxel v when one unit of intensity is emitted from beamlet b.

Model Assumption: We assume that the radiation delivery process can be represented by the linear map A. This means that no beamlet affects the deposition of another beamlet. However, this is a standard assumption within the radiation therapy and fluence optimization community. While patient outcome and tumor reduction may be much more complex and nonlinear, dose deposition is approximated to be linear within the research community.

Furthermore, there are simple restrictions on the dose delivered to each structure. No voxel in structure s can receive a dose greater than U^s_{max}, and no voxel in structure s can receive a dose less than L^s_{min}.

Finally, we have the decision variable y_b, which is the intensity of beamlet $b \; \forall \; b \in B$. We then construct model 3.1, which uses the $L2$ norm to minimize the total deviation from the target dose, subject to the minimum and maximum constraints.

$$\min \quad ||Ay - C||_2^2 \tag{3.1a}$$

$$\sum_{b \in B} a_{vb} y_b \leq U^s_{max} \qquad \forall v \in V^s, \quad s \in S \tag{3.1b}$$

$$\sum_{b \in B} a_{vb} y_b \geq L^s_{min} \qquad \forall v \in V^s, \quad s \in S \tag{3.1c}$$

$$y_b \geq 0 \qquad \forall \; b \in B \tag{3.1d}$$

Additional Constraints

The three primary types of constraints used are max dose constraints, mean dose constraints and dose-volume histogram (DVH) constraints. These constraints work by restricting various proportions of the structure. Max and min dose constraints constrain the dose on each voxel. Average dose constraints allow more variation within the structure, and DVH constraints are the most flexible and allow the treatment planner to finely constrain percentages of the tumor volume.

We have already mentioned max and min dose constraints in model 3.1. They restrict the maximum and minimum dose that can be delivered to each voxel within a structure, as shown in is done with constraints 3.2.

$$\sum_{b \in B} a_{vb} y_b \leq U^s_{max} \qquad \forall v \in V^s, \quad s \in S \tag{3.2a}$$

$$\sum_{b \in B} a_{vb} y_b \geq L^s_{min} \qquad \forall v \in V^s, \quad s \in S \tag{3.2b}$$

Mean dose constraints restrict the average dose delivered to an entire structure. Define U^s_{mean} and L^s_{mean} as the maximum and minimum average dose delivered to structure s, respectively (Equations 3.3).

$$\frac{\sum_{v \in V^s, b \in B} a_{vb} y_b}{|V^s|} \leq U^s_{mean} \qquad \forall s \in S \tag{3.3a}$$

$$\frac{\sum_{v \in V^s, b \in B} a_{vb} y_b}{|V^s|} \geq L^s_{mean} \qquad \forall s \in S \tag{3.3b}$$

Dose-Volume Histogram Constraints

Dose-Volume Histogram constraints are rooted in analysis of the Dose-Volume Histogram (Figure 3.2). A DVH plots the proportion of voxels against the dose that all these voxels receive. Note that in figure 3.2, target structures, such as the PTV, receive a high dose to most voxels, whereas OAR structures such as the Heart receive low dose for most voxels. DVH constraints aim to provide a less rigid formulation by permitting no more than $(1-\alpha)\%$ of voxels within structure s to receive a dose greater than the limit $U^{\alpha,s}_{dvh}$ [42]. For example, in the case of Figure 3.2, a treatment planner may decide that the current dose delivered to

the heart is too high. They can then dictate that no more than 10% of voxels in the Heart may receive a dose of 0.3 × Normalized Dose. This new constraint will push the purple line (Heart ROI) down while allowing the model to be flexible. A robust OAR may benefit from DVH constraints, as it allows a slightly higher dose to be delivered to a small proportion of voxels that can be healed quicker by the nearby healthy tissues in the OAR, which receive a lower dose. Furthermore, a planner can have multiple DVH constraints for a single structure s, thus narrowly defining dose delivery. Let $\mathcal{A}^s$ be set of all DVH constraints for structure s.

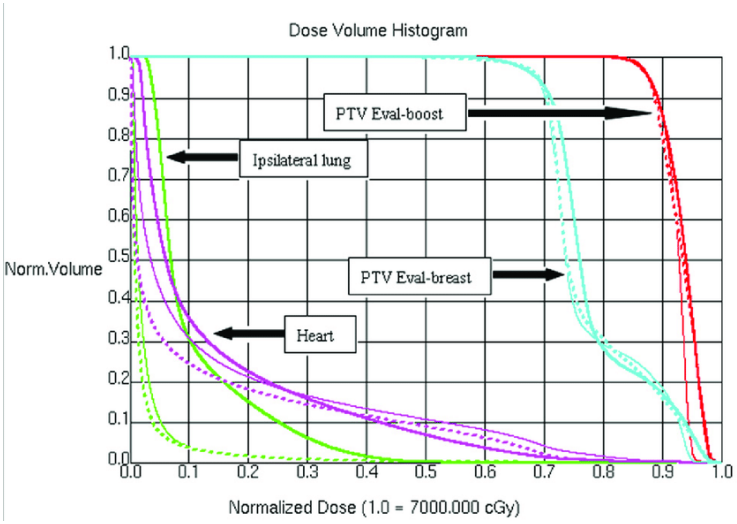

Figure 3.2: Example of a Dose-Volume Histogram [3]

DVH and average dose constraints are particularly important because treatment plans based solely on simple constraints, such as minimizing dose OARs and/or ensuring a minimum prescribed dose to the tumor, often fail to meet clinical approval. This originates from the observation that the resulting optimization models with the aforementioned simple constraints may lead to optimal solutions that occur in the boundary of the set of feasible (acceptable) solutions, where a constraint is satisfied as equality, often implying that the dose delivered to a structure attains its minimum or maximum allowable dose. Although the maximum (or minimum) dose is considered safe depending on the structure, this is not ideal; the preference is to obtain a "less extreme" solution to allow for inevitable variations in the model's parameter (that are often uncertain and hard to predict at the time of planning). Moreover, imposing DVH and average dose constraints allow for better distribution of the dose across the set of structures (i.e., PTV and OARs) [42].

The structure of a DVH constraint is nonlinear, and cannot be modeled without introducing binary variables or other sources of nonlinearity [42]. DVH constraints can be modeled,

but they require the introduction of integer dummy variables, which will make the model nonconvex, thereby increasing both the complexity of the model and the length of time that it takes to find the optimal solution.

The aforementioned paper by Romeijn et al. proposed a linear approximation that constrains the average dose received by the $(1-\alpha)$ voxels receiving the highest dose to be no more than $U_{dvh}^{\alpha,s}$. These conditional value-at-risk constraints bound the mean value of the tails rather than the entire tail (Figure 3.3).

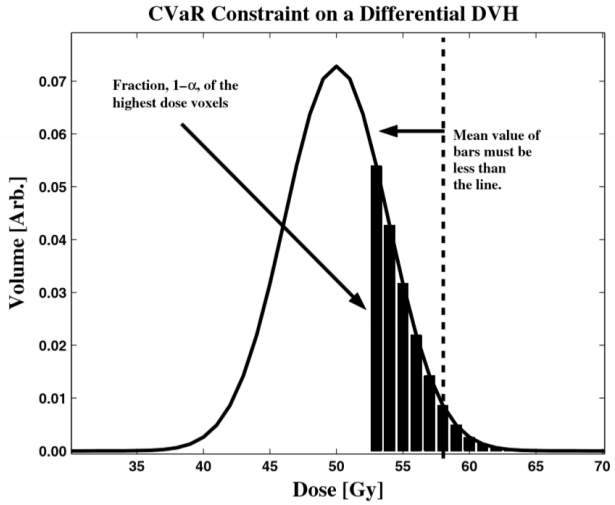

Figure 3.3: Demonstration of a Conditional Value-at-Risk Constraint [42].

These conditional value-at-risk constraints can be modeled linearly, and are common in the literature [42]. Mathematically, conditional value-at-risk constraints introduce the free decision variable $\bar{\zeta}^{\alpha,s}$ which, when the constraint is tight, corresponds to the minimum dose delivered to the $(1-\alpha)|V|$ voxels receiving the highest dose.

The model will balance the value of $\bar{\zeta}^{\alpha,s}$, in such a way that limits the dose delivered to the top proportion of voxels. A lower value will make the constraint looser, but if the value of $\bar{\zeta}^{\alpha,s}$ lowers too far, below the minimum value of the set of $(1-\alpha)$ voxels receiving the most dose, the variation on the second component of the left side of the constraint will begin to grow [42].

$$\bar{\zeta}^{\alpha,s} + \frac{1}{(1-\alpha)|V_s|} \sum_{v \in V^s} \max(0,\ -\bar{\zeta}^{\alpha,s} + \sum_{b \in B} a_{vb} y_b) \leq U_{dvh}^{\alpha,s} \qquad \forall\ \alpha \in \mathcal{A}^s,\ s \in S \tag{3.4}$$

This is easily linearized by introducing a dummy variable, although this increases the complexity of the model.

We then have the analogous lower bound DVH constraint that ensures that the average dose received by the $(1-\alpha)$ voxels receiving the lowest dose can be no less than $L_{dvh}^{\alpha,s}$

$$\zeta^{\alpha,s} - \frac{1}{(1-\alpha)|V_s|} \sum_{v \in V^s} \max(0,\ \zeta^{\alpha,s} - \sum_{b \in B} a_{vb} y_b) \geq L_{dvh}^{\alpha,s} \qquad \forall\ \alpha \in \mathcal{A}^s,\ s \in S \tag{3.5}$$

These can be linearized by introducing dummy variables τ_v and $\bar{\tau}_v$ as follows:

$$\bar{\zeta}^{\alpha,s} + \frac{1}{(1-\alpha)|V_s|} \sum_{v \in V^s} \bar{\tau}_v \leq U_{dvh}^{\alpha,s} \qquad \forall \alpha \in \mathcal{A}^s,\ s \in S \tag{3.6a}$$

$$\zeta^{\alpha,s} - \frac{1}{(1-\alpha)|V_s|} \sum_{v \in V^s} \tau_v \geq L_{dvh}^{\alpha,s} \qquad \forall \alpha \in \mathcal{A}^s,\ s \in S \tag{3.6b}$$

$$\bar{\tau}_v \geq -\bar{\zeta}^{\alpha,s} + \sum_{b \in B} a_{vb} y_b \qquad \forall v \in V^s,\ s \in S \tag{3.6c}$$

$$\tau_v \geq \bar{\zeta}^{\alpha,s} - \sum_{b \in B} a_{vb} y_b \qquad \forall v \in V^s,\ s \in S \tag{3.6d}$$

$$\tau_v, \bar{\tau}_v \geq 0 \qquad \forall v \in V^s,\ s \in S \tag{3.6e}$$

$$\bar{\zeta}^{\alpha,s}, \zeta^{\alpha,s} \quad free \qquad \forall \alpha \in \mathcal{A}^s,\ s \in S \tag{3.6f}$$

3.1.2 Conventional Radiation Therapy: Full Model

We can now write the full model for fluence map optimization of conventional radiation therapy:

$$\min \quad ||Ay - C||_2^2 \tag{3.7a}$$

$$\sum_{b \in B} a_{vb} y_b \leq U^s_{max} \qquad \forall v \in V \tag{3.7b}$$

$$\sum_{b \in B} a_{vb} y_b \geq L^s_{min} \qquad \forall v \in V \tag{3.7c}$$

$$\frac{\sum_{v \in V^s, b \in B} a_{vb} y_b}{|V^s|} \leq U^s_{mean} \qquad \forall s \in S \tag{3.7d}$$

$$\frac{\sum_{v \in V^s, b \in B} a_{vb} y_b}{|V^s|} \geq L^s_{mean} \qquad \forall s \in S \tag{3.7e}$$

$$\bar{\zeta}^{\alpha,s} + \frac{1}{(1-\alpha)|V_s|} \sum_{v \in V^s} \bar{\tau}_v \leq U^{\alpha,s}_{dvh} \qquad \forall \alpha \in \mathcal{A}^s, s \in S \tag{3.7f}$$

$$\zeta^{\alpha,s} - \frac{1}{(1-\alpha)|V_s|} \sum_{v \in V^s} \tau_v \geq L^{\alpha,s}_{dvh} \qquad \forall \alpha \in \mathcal{A}^s, s \in S \tag{3.7g}$$

$$\bar{\tau}_v \geq -\bar{\zeta}^{\alpha,s} + \sum_{b \in B} a_{vb} y_b \qquad \forall v \in V^s,\ s \in S \tag{3.7h}$$

$$\tau_v \geq \bar{\zeta}^{\alpha,s} - \sum_{b \in B} a_{vb} y_b \qquad \forall v \in V^s,\ s \in S \tag{3.7i}$$

$$y_b \geq 0 \qquad \forall b \in B \tag{3.7j}$$

$$\bar{\zeta}^{\alpha,s}, \zeta^{\alpha,s} \quad free \qquad \forall \alpha \in \mathcal{A}^s,\ s \in S \tag{3.7k}$$

$$\tau_v, \bar{\tau}_v \geq 0 \qquad v \in V^s, \forall s \in S \tag{3.7l}$$

3.2 Proposed SFRT Formulation

This general formulation is insufficient for SFRT because it fixes a specific target matrix C, which cannot change during the optimization. Current practice is for a treatment planner to select quality sphere positions and construct a target matrix based off of these fixed sphere positions where all points within spheres receive the peak dose and all points within the tumor and outside spheres receive the valley dose. However, our framework aims to be flexible, allowing us to optimize the sphere placement and the beamlet intensities simultaneously.

We accomplish this by tying the maximum independent set problem to the fluence optimization with the new objective function for the tumor. The new target dose matrix

must somehow be a function of x, as illustrated below:

$$||Ay - C(x)||_2^2 \tag{3.8}$$

Where the binary decision variable $x_i = 1$ if node i is selected as the center of a sphere $\forall i \in N$, and $x_i = 0$ otherwise.

3.2.1 Redefinition of Target Dose Matrix

For our new model, C is replaced by D, which is defined as a $|V| \times |N|$ matrix where d_{vi} is the dosage to be deposited in voxel v if i is selected for a radiation sphere, and 0 otherwise. Then, the operation Dx produces a $|V|$ dimensional column vector containing the prescribed dose for every voxel. For a voxel v within the tumor, the element $d_{vi} \in D$ would contain the peak-dose if that voxel is inside a node i where $x_i = 1$. Because the actual radiation sphere is 1.5 cm in diameter and the sphere centers must all be 3 cm apart, in accordance with the MIS, no feasible treatment plan can have two spheres target the same voxel. Thus, no target dose value for a voxel can receive value from two different entries in the D matrix in a feasible treatment plan.

This fits the requirements for voxels within the tumor, but does not work for voxels within OARs or voxels within the tumor that are not within a radiation sphere. So, in the D matrix, all entries are 0 for any voxels not specifically targeted for radiation delivery with a sphere. Thus, the objective function is modified to be

$$||Ay - (\rho Dx + \bar{D})||_2^2 \tag{3.9}$$

We define $\bar{D}$ to be a $|V|$ dimensional column vector with elements that are the target dosage of each voxel v in the set of OARs, and the valley dose for each voxel in the tumor.

The D matrix is extremely large, so to reduce file size, D only stores values between 0 and 1. Entries are 1 if the voxel is completely within the sphere and 0 otherwise. Next, we introduce a scalar ρ = (peak dose - valley dose), and multiply it by D, so that any voxel within a sphere will be prescribed ((peak dose - valley dose) + valley dose), from D and $\bar{D}$, respectively.

Finally, we add a level of complexity by modifying D to be a proportional dose matrix.

This means that the value of the element at index i, v is the proportion of voxel v that sits within sphere i. Each of these values will be between zero and one. Actual SFRT delivery does not include a steep dose falloff. When the dose is tracked spatially between two sphere centers, peak dose is primarily delivered to the center of a sphere, and the dose gradually falls off towards the midpoint between two spheres, which is the point where the true valley dose is measured in conventional SFRT treatment plan analysis. By using the proportionality matrix, we better approximate and plan for this gradual dose falloff between sphere centers (Figure 3.4b).

To calculate D, we have to calculate the volume of the intersection between a sphere and a rectangular prism. This is a difficult problem with no simple closed form solution. It requires complex, time intensive integrations over complex and ill defined boundaries. If the voxels and spheres sat on a consistent grid, this could be simple, as the calculation could be done for a single sphere and its surrounding voxels, and the results could be re-centered for each candidate sphere. However, there is no guarantee that the candidate sphere grid will line up cleanly with the voxel grid. This is because the positions of the nodes will be found using Algorithm 1 but the positions of the voxels will be found using the PortPy library, as discussed later, in the Data section. Thus, rather than calculating the actual volume, we have elected for an approximation, where we discretize each voxel into fractions and calculate the number of these points that sit within the sphere, as shown in Figure 3.4.

Model Assumption/Limitation: We do not precisely calculate the volume of each voxel that lies within each sphere. This introduces bias into the model parameters, but we assume that the resulting treatment plans will be similar.

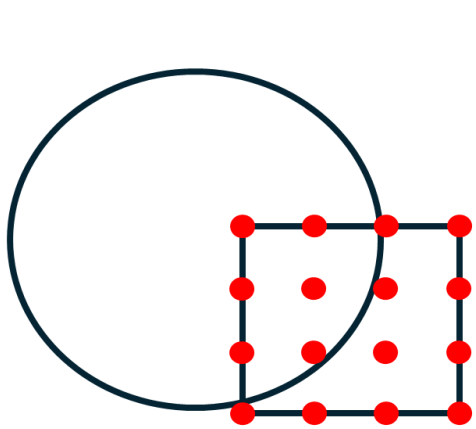

(a) 2D visualization of D matrix calculation: The voxel is discretized into points, and the matrix element represents the fraction of those within the tumor.

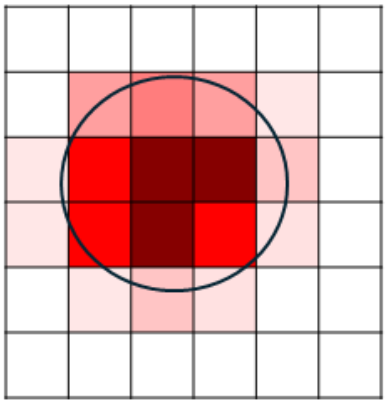

(b) Dose prescription visualization: Dark voxels are fully within the target and receive a value of 1; partial voxels receive a fractional value.

Figure 3.4: Illustration of the D matrix construction and its implications for dose prescription based on spatial voxel overlap.

3.2.2 New Model

Using this modified objective function, we can write the new model as follows:

$$\min \quad ||Ay - (\rho Dx + \bar{D})||_2^2 \tag{3.10a}$$

$$\max \quad \sum_{i \in N} x_i \tag{3.10b}$$

$$x_i + x_j \leq 1 \qquad \forall (i,j) \in E \tag{3.10c}$$

$$\sum_{b \in B} a_{vb} y_b \leq U^s_{max} \qquad \forall v \in V \tag{3.10d}$$

$$\sum_{b \in B} a_{vb} y_b \geq L^s_{min} \qquad \forall v \in V \tag{3.10e}$$

$$\frac{\sum_{v \in V^s, b \in B} a_{vb} y_b}{|V^s|} \leq U^s_{mean} \qquad \forall s \in S \tag{3.10f}$$

$$\frac{\sum_{v \in V^s, b \in B} a_{vb} y_b}{|V^s|} \geq L^s_{mean} \qquad \forall s \in S \tag{3.10g}$$

$$\bar{\zeta}^{\alpha,s} + \frac{1}{(1-\alpha)|V_s|} \sum_{v \in V^s} \bar{\tau}_v \leq U^{\alpha,s}_{dvh} \qquad \forall \alpha \in \mathcal{A}^s,\ s \in S \tag{3.10h}$$

$$\zeta^{\alpha,s} - \frac{1}{(1-\alpha)|V_s|} \sum_{v \in V^s} \tau_v \geq L^{\alpha,s}_{dvh} \qquad \forall \alpha \in \mathcal{A}^s,\ s \in S \tag{3.10i}$$

$$\bar{\tau}_v \geq -\bar{\zeta}^{\alpha,s} + \sum_{b \in B} a_{vb} y_b \qquad \forall v \in V^s,\ s \in S \tag{3.10j}$$

$$\tau_v \geq \bar{\zeta}^{\alpha,s} - \sum_{b \in B} a_{vb} y_b \qquad \forall v \in V^s,\ s \in S \tag{3.10k}$$

$$x_i \in \{0,1\} \qquad \forall i \in N \tag{3.10l}$$

$$y_b \geq 0 \qquad \forall b \in B \tag{3.10m}$$

$$\bar{\zeta}^{\alpha,s}, \zeta^{\alpha,s} \quad free \qquad \forall \alpha \in \mathcal{A}^s,\ s \in S \tag{3.10n}$$

$$\tau_v, \bar{\tau}_v \geq 0 \qquad \forall v \in V^s,\ s \in S \tag{3.10o}$$

However, a mathematical program cannot have two objective functions, so the model must be augmented so that both objectives are represented in a single objective function. The simplest method is to merely combine the two models with a hyperparameter λ, creating the new objective function:

$$\max \quad \lambda \sum_{i \in N} x_i - ||Ay - (\rho Dx + \bar{D})||_2^2 \tag{3.11}$$

However, this model will be very sensitive to changes in the parameter λ, because the two objective functions are in direct competition. Generally, fluence map optimization will result in a better solution if less radiation is delivered, since the prescriptions for the OARs will be less than the tumor prescription. Thus, the fluence term will always attempt to minimize the size of the MIS.

We decided to use an alternative objective function that minimizes the deviation from the prescribed dose, but we add a constraint so that the model must place at least ϕ spheres (Equation 3.12).

$$\sum_{i \in N} x_i \geq \phi \tag{3.12}$$

This allows us to leverage a key structural element in the model: The fluence optimization is completely convex. This allows us to solve the MIS model shown in Chapter 2, use the size of the maximum independent set to define ϕ, and use the actual MIS to warm start the much larger proposed model.

One of the most common techniques used to solve integer and mixed integer linear programs is branch and bound. This method relaxes the integrality constraints of the initial problem and then splits the problem into multiple parts or "branches" which attempt to find the optimal integer solution by adding cuts. This process can be very slow, and it can be very difficult to find any integer solution, much less a quality solution. By warm starting all integer variables, we can radically speed up the branch and bound algorithm.

To accentuate the speed of the fluence optimization, we linearize the objective function using the $L1$ norm by introducing the dummy variable z_v, defined as the $|V|$ dimensional column vector z. This is done in the literature with conventional radiation therapy treatment planning [42]. Using the new objective function gives the following model:

3.2.3 Full Linearized Model

$$
\begin{aligned}
\min \quad & \sum_{v \in V} z_v && && (3.13a)\\
& z \geq Ay - (\rho Dx + \bar{D}) && && (3.13b)\\
& z \geq -(Ay - (\rho Dx + \bar{D})) && && (3.13c)\\
& \sum_{i \in N} x_i \geq \phi && && (3.13d)\\
& x_i + x_j \leq 1 && \forall (i,j) \in E && (3.13e)\\
& \sum_{b \in B} a_{vb} y_b \leq U^s_{max} && \forall v \in V && (3.13f)\\
& \sum_{b \in B} a_{vb} y_b \geq L^s_{min} && \forall v \in V && (3.13g)\\
& \frac{\sum_{v \in V^s, b \in B} a_{vb} y_b}{|V^s|} \leq U^s_{mean} && \forall s \in S && (3.13h)\\
& \frac{\sum_{v \in V^s, b \in B} a_{vb} y_b}{|V^s|} \geq L^s_{mean} && \forall s \in S && (3.13i)\\
& \bar{\zeta}^{\alpha,s} + \frac{1}{(1-\alpha)|V_s|} \sum_{v \in V^s} \bar{\tau}_v \leq U^{\alpha,s}_{dvh} && \forall \alpha \in \mathcal{A}^s,\ s \in S && (3.13j)\\
& \zeta^{\alpha,s} - \frac{1}{(1-\alpha)|V_s|} \sum_{v \in V^s} \tau_v \geq L^{\alpha,s}_{dvh} && \forall \alpha \in \mathcal{A}^s,\ s \in S && (3.13k)\\
& \bar{\tau}_v \geq -\bar{\zeta}^{\alpha,s} + \sum_{b \in B} a_{vb} y_b && \forall v \in V^s,\ s \in S && (3.13l)\\
& \tau_v \geq \bar{\zeta}^{\alpha,s} - \sum_{b \in B} a_{vb} y_b && \forall v \in V^s,\ s \in S && (3.13m)\\
& x_i \in \{0,1\} && \forall i \in N && (3.13n)\\
& y_b \geq 0 && \forall b \in B && (3.13o)\\
& z_v \quad free && \forall v \in V && (3.13p)\\
& \tau_v, \bar{\tau}_v \geq 0 && \forall v \in V^s,\ s \in S && (3.13q)\\
& \bar{\zeta}^{\alpha,s}, \zeta^{\alpha,s} \quad free && \forall \alpha \in \mathcal{A}^s,\ s \in S && (3.13r)\\
& && && (3.13s)
\end{aligned}
$$

Note that since z is bounded in positive and negative directions in constraints 3.13b-c, z can be a free variable and will always be non-negative.

Because there are two conflicting objective functions with no clear way of identifying the proper weighting scheme, we propose an algorithm that finds the MIS, and sets the size of the MIS as the value of ϕ. Then, once a quality solution is reached, the model can be reran with the value of $\phi - 1$, and so on as time allows. This will provide a set of treatment plan options that a medical professional can choose from, since it may be beneficial to reduce the number of spheres for the sake of less tissue damage.

3.3 Data

Calculating and defining sample parameters is difficult. There are structural parameters, such as the set of voxels and structures, which can be derived from the CT scan, and there are prescribed parameters, such as the beamlets, max/min, average, and dvh constraints as well as the prescribed dose for each structure, and these can be obtained by consulting with a medical professional, but the influence matrix A is more difficult to calculate. This matrix contains the dose deposited to every voxel from every beamlet. The number of voxels in a tumor can easily number over a quarter million depending on the size of the voxels, and the number of beamlets can easily number in the tens of thousands. This creates a massive matrix, that is difficult to work with. The raw pickle (.pkl) files containing the D matrix and the A matrix can easily be 13GB each. Compressed matrix format (csr matrices) are necessary to keep the models manageable. Thankfully, both of these matrices are sparse, so their sparse matrices are much more manageable.

Calculating the A matrix is very difficult. It requires complex physics calculations of the dose deposition of the beamlet as it passes through many tissues, each of which has a different absorption profile. Because of this, it was determined that the calculation of the dose deposition matrix is not within the scope of this project. However, finding the dose deposition matrix from other sources was difficult as well. We were unable to find anywhere in the standard clinical treatment planning software where this matrix could be exported. It is possible that this software uses metaheuristic methods to calculate beamlet intensities, as this would enable the software to find a solution without having to do extensive the preprocessing required by the A matrix calculation.

Thankfully, PortPy has the capability to calculate this matrix. PortPy contains methods that can efficiently calculate the dose deposition matrix.

Using this dataset, we can use the PortPy library to create the PTV-Grid boundary, which is the PTV that has been shrunk so that the entire volume of any sphere with its center within PTV-Grid will lie within the PTV. This is done in PortPy by shrinking the PTV ROI by 0.8 cm. Then, the set of voxels for each structure and a curated set of beamlets can be extracted using PortPy. PortPy also has a set of clinical criteria that includes max/min, average, and dvh constraints, as well as the prescribed dose for each ROI. Using the CT scan with the PTV-Grid ROI, the nodes and edges required by the MIS problem can be extracted to identify all the candidate locations for sphere centers. The last step is to extract the D matrix. The size and locations of the voxels are known from PortPy, and the size locations of the spheres are known, so this calculation is done as discussed above in section 3.2.1.

SFRT is effective for large and bulky tumors, but the PortPy library of 50 lung tumors contains tumors of all sizes. To this end, we have selected 20 tumors that are ideal candidates for SFRT and will be used for our experiments (Table 2.2).

The last piece of complexity is the downsampling of voxels. The default size of a voxel in Portpy is $1 \times 1 \times 2.5$ mm, but this makes the model very computationally expensive. Portpy has a downsampling feature that will allow the size of the voxels to change, and the influence matrix and all other parameters with it. We have enlarged the voxels on each slice by a factor of 5 in order to create a reasonably sized model. Thus, the final voxel size is $5 \times 5 \times 2.5$ mm.

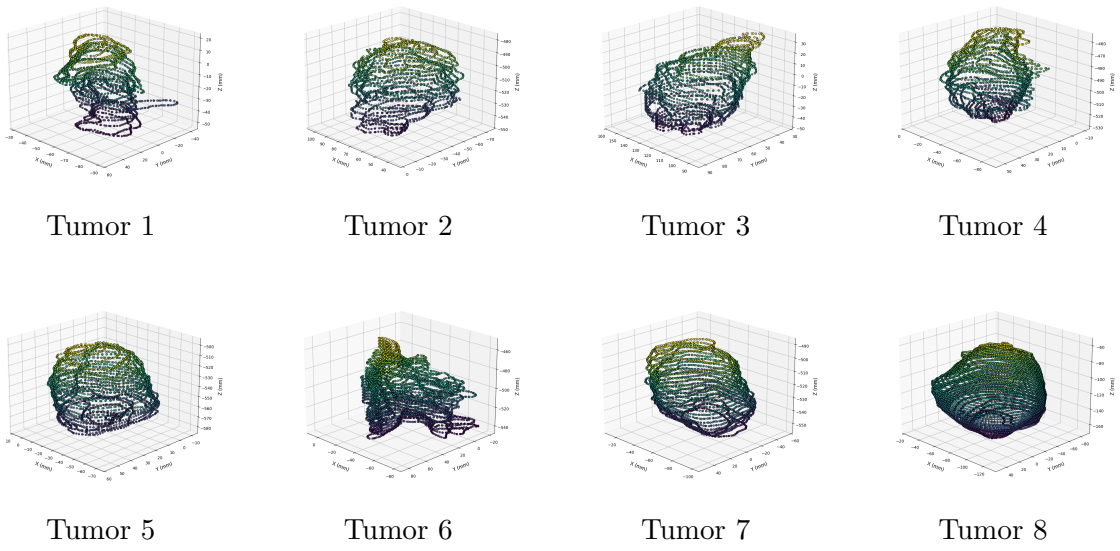

Tumor 1 Tumor 2 Tumor 3 Tumor 4

Tumor 5 Tumor 6 Tumor 7 Tumor 8

Figure 3.5: Patient PTV Visualization

3.3.1 Toy Model

Due to the complex 3-dimensional geometry of the tumor and the sphere, it is difficult to validate the optimization model visually. To accomplish this, we have constructed a 2-dimensional toy model that can be easily validated. The toy model contains three OARs and one tumor, as shown in Figure 3.6. The tumor is in red and pink. The red section is where a node can be centered at, and a sphere can extend out into the pink section.

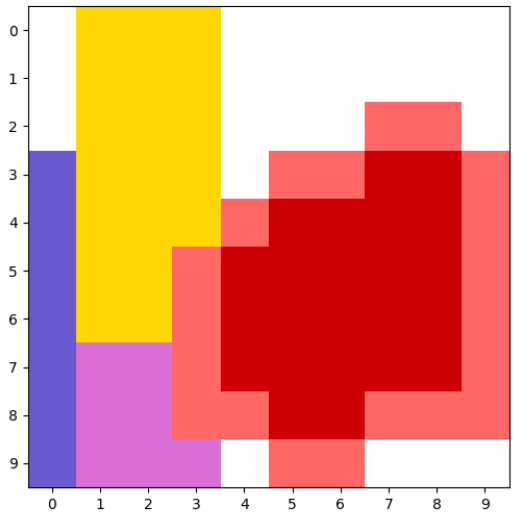

Figure 3.6: Structures for Toy Model

The toy model only includes a single beam, which fires from left to right. This beam is divided into 10 beamlets, each of these beamlets is shown in Figure 3.7.

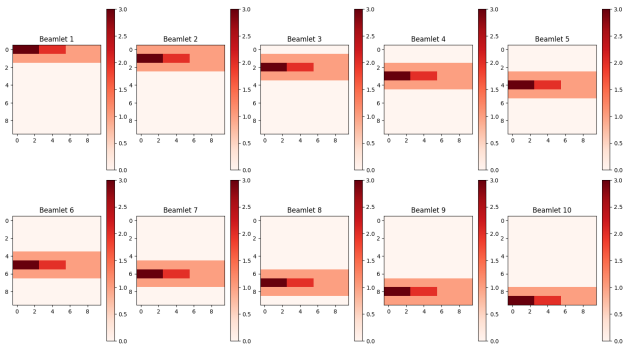

Figure 3.7: Set of Beamlets for Toy Model

We define a candidate sphere center at the center of each voxel within the tumor. Each "sphere" takes the shape of a cross, where each sphere includes the four voxels adjacent to itself. Each of these spheres must be at least three squares away from each other. Two different treatment plans were created to compare(Table 3.3, Table 3.4). They both share the same prescriptions (Table 3.2), but treatment plan B assumes that OAR 2 (Purple) is sensitive to radiation and needs to receive less dose. Treatment plan B includes an extra DVH constraint in order to reduce dose to OAR 2 while maintaining the flexibility of the model (Table 3.4).

Structure	Color	Prescription
Peak Tumor Dose	Red/Pink	30 Gy
Valley Tumor Dose	Red/Pink	6 Gy
OAR 1	Yellow	5 Gy
OAR 2	Purple	1 Gy
OAR 3	Indigo	2 Gy

Table 3.2: Toy Model Dose Prescription

Structure	Max Dose	Max Average Dose	DVH Max
OAR 1	10 Gy	4 Gy	30%, 6 Gy
OAR 2	11 Gy	5 Gy	-
OAR 3	12 Gy	-	-

Table 3.3: Treatment Plan A: Toy Model Dose Constraints

Structure	Max Dose	Max Average Dose	DVH Max
OAR 1	10 Gy	4 Gy	30%, 3 Gy
OAR 2	11 Gy	5 Gy	30%, 4 Gy
OAR 3	12 Gy	-	-

Table 3.4: Treatment Plan B: Toy Model Dose Constraints

Chapter 4

Results

4.1 Toy Model Results

Optimal sphere locations and fluences were calculated for treatment plans A and B. The MIS size was 4 for the tumor and results are shown for both treatment plans for all four different minimum node placements. In every situation, the minimum number of nodes were placed, so if the value of ϕ was 3, 3 spheres were placed for every value of ϕ.

4.1.1 Treatment Plan A

Table 4.1 shows the deviation from the prescription and total dose delivered to all structures for various numbers of sphere placements. Deviation and total dose delivery both increase as the number of spheres increases.

Table 4.1: Treatment Plan A: Toy Model Results

Number of Nodes	Deviation	Total Dose Delivered
4	802.12 Gy	367.62 Gy
3	641.85 Gy	363.24 Gy
2	494.94 Gy	338.83 Gy
1	351.16 Gy	333.50 Gy

Figure 4.1 shows the optimal dose delivery and deviation from the prescribed dose for all numbers of sphere placements for treatment plan A. The deviation is high for all treatment

plans within the spheres. This is due to the small set of beamlets. In actual radiation therapy treatment, the set of beamlets and beam angles are much more comprehensive.

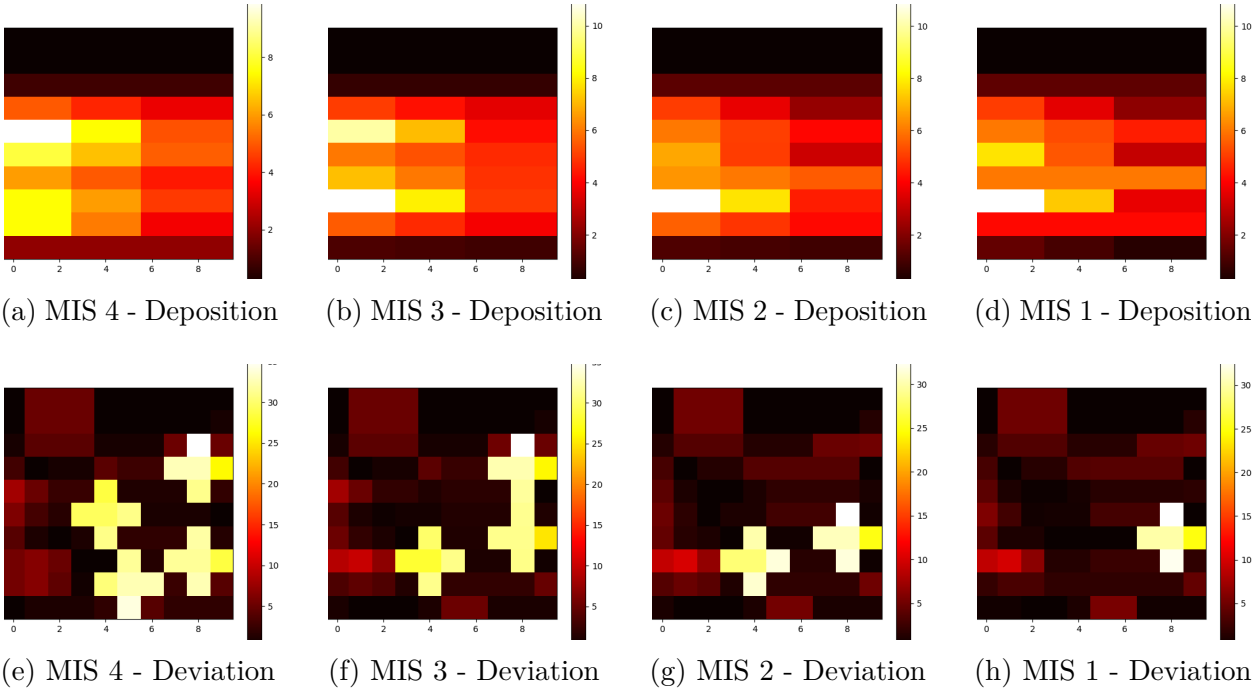

(a) MIS 4 - Deposition (b) MIS 3 - Deposition (c) MIS 2 - Deposition (d) MIS 1 - Deposition

(e) MIS 4 - Deviation (f) MIS 3 - Deviation (g) MIS 2 - Deviation (h) MIS 1 - Deviation

Figure 4.1: Toy Model Optimization Results for Treatment Plan A

4.1.2 Treatment Plan B

Treatment plan B adds a DVH constraint to reduce the dose to the OAR in front of the bottom of the tumor. This pushes the dose, and the spheres higher in the tumor, as seen when only placing one sphere within the tumor (Figure 4.2). However, this constraint is very restrictive. When treatment plan B places four nodes, the resultant beamlets are identical to those from the placement of three beamlets (Table 4.2). This is because the dose is so heavily restricted that although an extra node is placed, no additional radiation delivery occurs. In actual radiation therapy, this effect is mitigated by a greater selection of beamlets and beam angles, as well as expert constraint selection.

Table 4.2: Treatment Plan B: Toy Model Results

Number of Nodes	Deviation	Total Dose Delivered
4	801.82 Gy	315.56 Gy
3	651.82 Gy	315.56 Gy
2	501.55 Gy	315.21 Gy
1	355.02 Gy	296.05 Gy

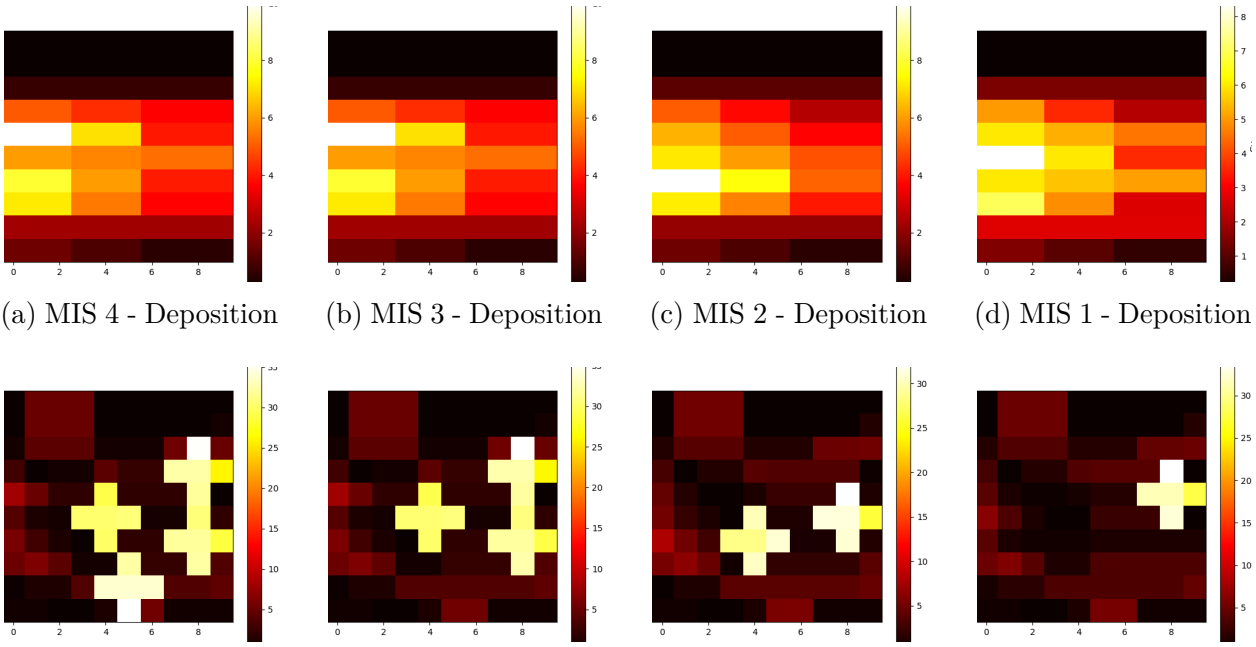

(a) MIS 4 - Deposition (b) MIS 3 - Deposition (c) MIS 2 - Deposition (d) MIS 1 - Deposition

(e) MIS 4 - Deviation (f) MIS 3 - Deviation (g) MIS 2 - Deviation (h) MIS 1 - Deviation

Figure 4.2: Toy Model Optimization Results for Treatment Plan B

These visualizations demonstrate the efficacy of the model. As long as all of the parameters entered into the model are accurate and high-quality, the resultant optimal solution will result in a high quality treatment plan.

4.2 PortPy Tumor Results

The SFRT Fluence Optimization Model from Chapter 3 was ran on the OSCER supercomputer for 40 hours. Results of this optimization are shown in Table 4.3. Recorded are the patient ID, as well as the respective PortPy ID number. The sizes of the tumor and overall CT are

also recorded in voxel and cm^3 units. The patients in Table 4.3 are sorted for PTV volume for a changing number of spheres placed. The optimality gap after 40 hours is recorded. Optimization models generally find an upper bound on the optimal solution, meaning that it is guaranteed that no solution can be better than a given value. The ratio between the current solution and this bound is known as the optimality gap. As the optimization progresses, this gap reduces as the current solution converges to the best bound. The deviations for all ROIs are also recorded, as well as the average deviation across all structures and the total run time of the model.

Patient ID	PortPy ID	PTV Volume	Candidate Spheres	PTV Voxels	Total Voxels	**Number of Spheres**	Optimality Gap	GTV Dev	PTV Dev	Esophagus Dev	Heart Dev	Left Lung Dev	Right Lung Dev	Spinal Cord	Skin Dev	Body Dev	**Average Deviation**	Run Time
1	4	312.6	273	5298	159110	**10**	0.6326	14.85	16.32	13.99	0.79	11.98	5.08	18.97	10.36	8.98	**9.009245**	40hr
1	4	312.6	273	5298	159110	**9**	0.6753	14.81	16.3	14.04	0.79	11.98	5.07	18.98	10.36	8.98	**9.011719**	40hr
1	4	312.6	273	5298	159110	**8**	0.7159	14.87	16.36	14.05	0.79	11.98	5.06	18.98	10.37	8.99	**9.015967**	40hr
2	22	348.3	334	5739	136503	**10**	0.7463	7.83	11.24	6.29	1.32	6.82	8.62	30.87	6.29	6.96	**6.964249**	40hr
2	22	348.3	334	5739	136503	**9**	1.1578	7.57	10.92	6.44	1.32	6.81	8.61	30.8	6.31	6.96	**6.960831**	40hr
2	22	348.3	334	5739	136503	**8**	1.0512	6.73	10.77	6.3	1.32	6.75	8.63	30.87	6.3	6.95	**6.952479**	40hr
3	14	357.2	371	5930	166986	**10**	0.7713	7.87	7.19	8.95	11.21	6.16	8.17	23.03	7.66	7.75	**7.745932**	40hr
3	14	357.2	371	5930	166986	**9**	0.8686	7.43	7.01	8.92	11.2	6.14	8.17	23.03	7.66	7.74	**7.739643**	40hr
3	14	357.2	371	5930	166986	**8**	0.8198	7.34	6.9	8.9	11.22	6.1	8.15	23.03	7.66	7.74	**7.73462**	40hr
4	17	372.6	360	6177	125451	**11**	0	5.48	7.43	8.49	-	7.62	5.68	16.28	5.93	5.29	**5.305807**	40hr
4	17	372.6	360	6177	125451	**10**	1.7454	5.1	7.3	8.63	-	7.62	5.69	16.21	5.95	5.29	**5.306692**	40hr
4	17	372.6	360	6177	125451	**9**	1.6543	4.58	7.03	8.64	-	7.63	5.68	16.18	5.95	5.27	**5.293583**	40hr
5	25	476.3	580	7739	187217	**14**	1.2778	8.09	7.81	5.52	12.14	11.76	6.45	24.95	7.78	7.48	**7.48184**	40hr
5	25	476.3	580	7739	187217	**13**	1.2517	7.98	7.74	5.52	12.14	11.76	6.45	24.95	7.78	7.48	**7.478965**	40hr
5	25	476.3	580	7739	187217	**12**	1.2140	7.86	7.66	5.51	12.14	11.76	6.45	24.95	7.78	7.47	**7.476129**	40hr
6	21	662.6	538	10818	185072	**17**	1.253	8.56	9.8	10.25	5.82	8.56	7.49	15.59	10.13	8.07	**8.08686**	40hr
6	21	662.6	538	10818	185072	**16**	1.2793	8.44	9.73	10.26	5.82	8.56	7.48	15.6	10.14	8.07	**8.083416**	40hr
6	21	662.6	538	10818	185072	**15**	1.25	8.36	9.67	10.26	5.82	8.56	7.48	15.6	10.13	8.06	**8.080314**	40hr
7	24	733.2	908	11717	191620	**21**	1.8096	5.57	6.04	13.9	9.74	12.31	5.67	24.88	8.89	7.82	**7.820815**	40hr
7	24	733.2	908	11717	191620	**20**	1.8021	5.4	5.9	13.94	9.72	12.31	5.66	24.92	8.9	7.82	**7.817411**	40hr
7	24	733.2	908	11717	191620	**19**	1.7419	5.32	5.84	13.95	9.71	12.31	5.65	24.91	8.9	7.81	**7.814473**	40hr
8	15	1276.9	2213	19769	212366	**42**	2.0098	4.57	6.32	7.89	9.29	13.7	9.11	35.33	12.29	10.68	**10.68239**	40hr
8	15	1276.9	2213	19769	212366	**41**	2.0096	4.56	6.26	8.01	9.26	13.72	9.08	35.33	12.3	10.68	**10.68133**	40hr
8	15	1276.9	2213	19769	212366	**39**	1.9832	4.43	6.21	7.94	9.27	13.69	9.07	35.35	12.32	10.67	**10.67683**	40hr

Table 4.3: Deviation from Prescribed dose for Patients and ROIs

Variation Across Tumor Size: Overall, average deviation (total deviation/$|V|$) does not change significantly across tumor sizes (Figure 4.3b). This demonstrates the effectiveness of our model for even very large (1276.9 cm^3) tumors. Interestingly, while there is no significant trend, PTV deviation also does not have a clear correlation with tumor size (Figure 4.3a).

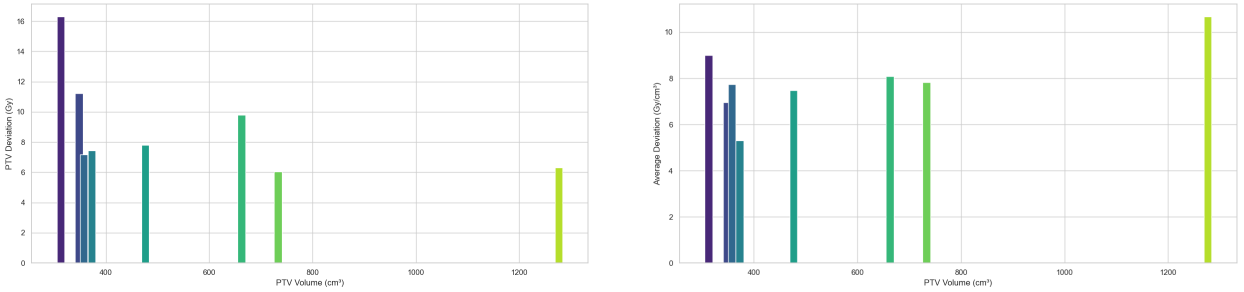

(a) PTV deviation across tumor volumes (b) Average Deviation across tumor volumes

Figure 4.3: Variation in Deviation Across Tumor Size

Variation Between MIS sizes: In almost all of the patients, total deviation increases as the number of spheres increases (Figure 4.4). This is expected because an increase in the number of spheres corresponds to an increase in the total dose prescribed to the tumor. Since the peak dose prescribed to the tumor is much higher than any prescription for an OAR, an increase in the number of spheres is likely to increase the total deviation, since either an OAR will receive more dose in order to meet the demands of the tumor, thus increasing deviation in the OARs, or the OAR will continue to have a lower dose and the prescription for that sphere will not be met, increasing the deviation in the PTV. The only exception to this rule comes in the smallest patient within our dataset (Figure 4.4a). The change in deviation is very small for this outlier, so this could be a product of the optimality gap.

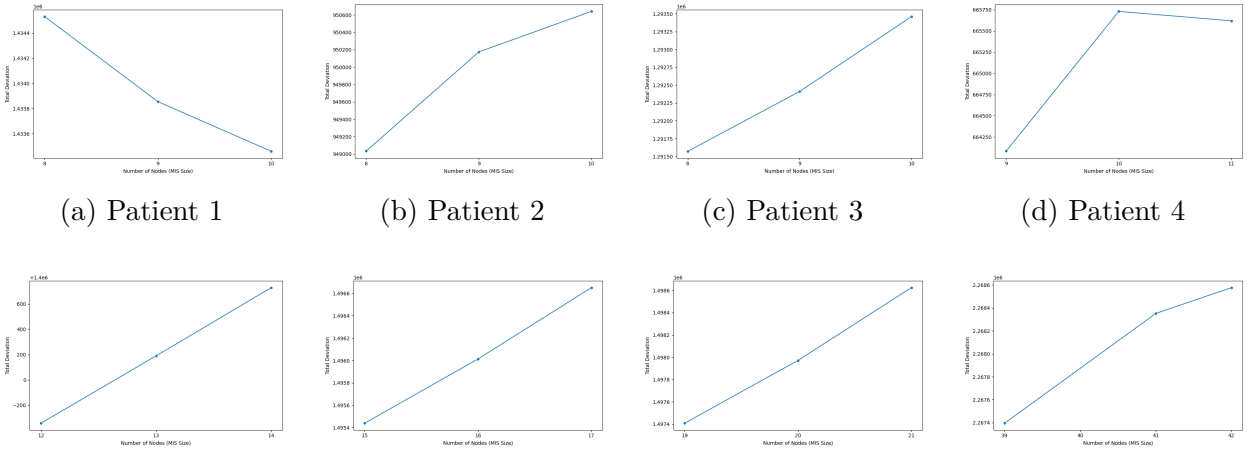

(a) Patient 1 (b) Patient 2 (c) Patient 3 (d) Patient 4

(e) Patient 5 (f) Patient 6 (g) Patient 7 (h) Patient 8

Figure 4.4: Total Dose Deviation Across Numbers of Spheres

When comparing OAR deviations across different tumor sizes, no simple patterns emerge (Figure 4.5). The only things of note are that deviation in the two lungs tend to most strongly

correlate with the number of nodes, and the Esophagus seems to vary more wildly than the others. The variance in the Esophagus is likely due to its small size, it is one of the smallest ROIs, so the numbers are more likely to be more variable to large changes in a small number of voxels. Notably, this erraticism primarily consists in less than a 5% change in average dose deviation.

The deviation in the lungs most strongly correlates with the number of nodes because the tumors are lung tumors. Thus, all tumors are very close to the lung, so as dose increases, the dose often must pass through the lung in order to reach the tumor, which will increase dose and increase deviation in the lung.

This lack of a clear pattern implies that as the prescription changes, the model will adjust and distribute dose across different OARs as necessary.

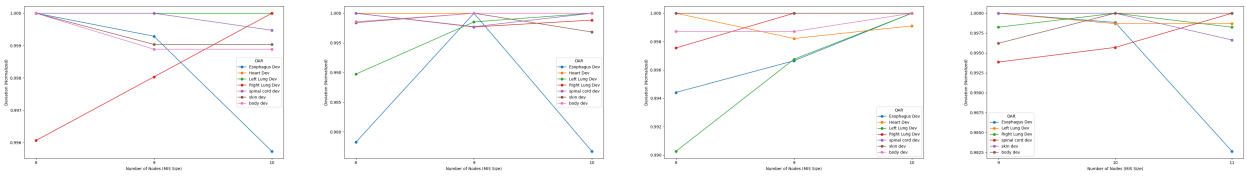

(a) Patient 1 (b) Patient 2 (c) Patient 3 (d) Patient 4

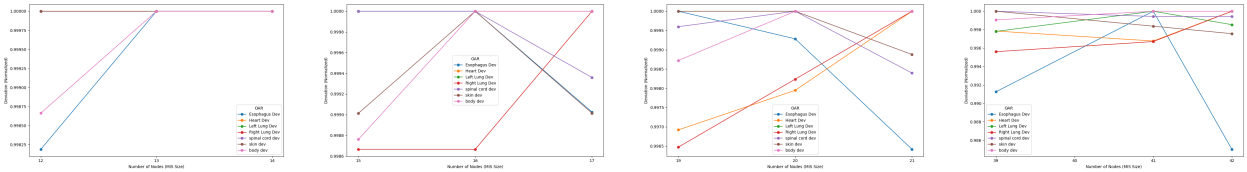

(e) Patient 5 (f) Patient 6 (g) Patient 7 (h) Patient 8

Figure 4.5: OAR Dose Deviation Across Number of Spheres

The strongest correlations between changes in the number of spheres and deviation in a ROI are PTV and GTV deviation. A greater number of spheres means more dose prescribed to the tumor. This is clearly shown in Figure 4.6, as all patients with the exception of patient 1 show a clear increase in deviation as OAR deviation increases. This makes sense, as it is more difficult to deliver a higher dose within the limits of the constraints and the OAR prescriptions, so as the number of spheres and total dose increases, the optimal plan is more likely to under deliver radiation.

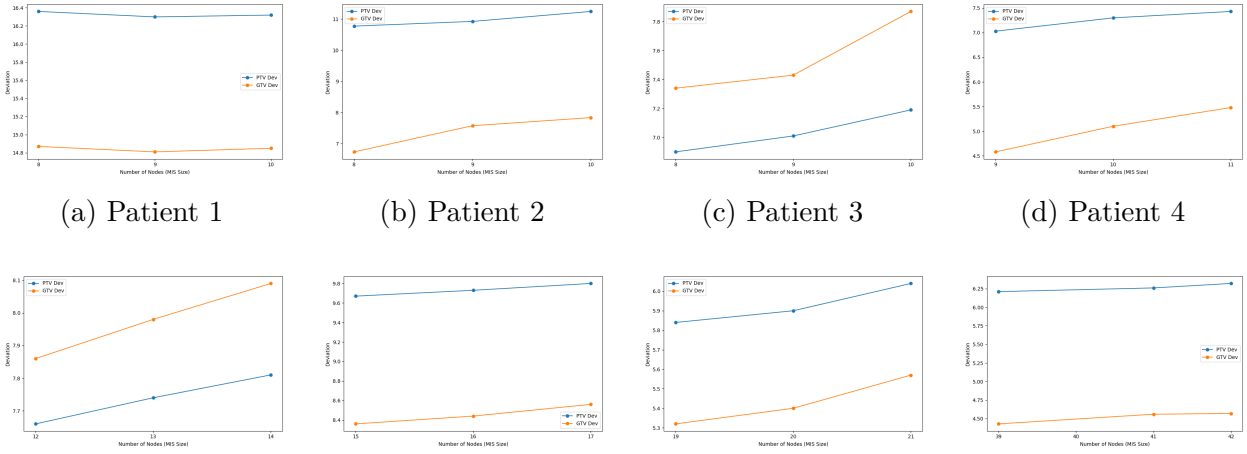

(a) Patient 1 (b) Patient 2 (c) Patient 3 (d) Patient 4

(e) Patient 5 (f) Patient 6 (g) Patient 7 (h) Patient 8

Figure 4.6: Tumor (PTV and GTV) Dose Deviation Across Number of Spheres

Time Considerations: Forty hours is a very long time to wait in the treatment planning process, so this length of time may not be feasible for actual delivery. Thus, experiments were ran for 8 hours in order to determine the quality of a solution after a more reasonable amount of time (Table 4.4).

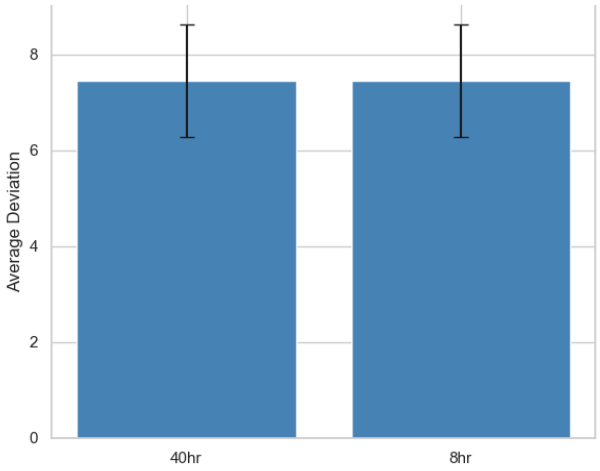

Figure 4.7: Average Deviation for 40 hour and 8 hour Experiments

Patient ID	PortPy ID	PTV Volume	Candidate Spheres	PTV Voxels	Total Voxels	**Number of Spheres**	Optimality Gap	GTV Dev	PTV Dev	Esophagus Dev	Heart Dev	Left Lung Dev	Right Lung Dev	Spinal Cord	Skin Dev	Body Dev	**Average Deviation**	Run Time
1	4	312.6	273	5298	159110	**10**	0.4408	13.38	15.67	14.07	0.79	11.97	5.05	19.01	10.37	8.96	**8.992382**	8hr
1	4	312.6	273	5298	159110	**9**	0.6851	14.81	16.3	14.04	0.79	11.98	5.07	18.98	10.36	8.98	**9.011719**	8hr
1	4	312.6	273	5298	159110	**8**	0.7327	14.87	16.36	14.05	0.79	11.98	5.06	18.98	10.37	8.99	**9.015967**	8hr
2	22	348.3	334	5739	136503	**10**	1.152	7.83	11.24	6.29	1.32	6.82	8.62	30.87	6.29	6.96	**6.964249**	8hr
2	22	348.3	334	5739	136503	**9**	1.2408	7.69	11.15	6.3	1.32	6.82	8.63	30.88	6.3	6.96	**6.964777**	8hr
2	22	348.3	334	5739	136503	**8**	1.234	7.37	10.89	6.42	1.32	6.8	8.64	30.86	6.31	6.96	**6.964649**	8hr
3	14	357.2	371	5930	166986	**10**	0.9577	7.66	7.16	0.85	11.2	6.17	8.15	23.03	7.66	7.75	**7.747103**	8hr
3	14	357.2	371	5930	166986	**9**	0.9215	7.35	7	8.88	11.2	6.12	8.15	23.03	7.66	7.75	**7.742389**	8hr
3	14	357.2	371	5930	166986	**8**	0.88	7.02	6.86	8.9	11.2	6.12	8.16	23.03	7.66	7.74	**7.738438**	8hr
4	17	372.6	360	6177	125451	**11**	0.8942	5.32	7.41	8.57	-	7.62	5.73	16.22	5.94	5.29	**5.308585**	8hr
4	17	372.6	360	6177	125451	**10**	1.761	5.1	7.3	8.63	-	7.62	5.69	16.21	5.95	5.29	**5.306692**	8hr
4	17	372.6	360	6177	125451	**9**	1.88	4.9	7.17	8.66	-	7.63	5.63	16.26	5.96	5.29	**5.304686**	8hr
5	25	476.3	580	7739	187217	**14**	79.2377	8.09	7.81	5.52	12.14	11.76	6.45	24.95	7.78	7.48	**7.48184**	8hr
5	25	476.3	580	7739	187217	**13**	79.2297	7.98	7.74	5.52	12.14	11.76	6.45	24.95	7.78	7.48	**7.478965**	8hr
5	25	476.3	580	7739	187217	**12**	125.23%	7.86	7.66	5.51	12.14	11.76	6.45	24.95	7.78	7.47	**7.476129**	8hr
6	21	662.6	538	10818	185072	**17**	1.3028	8.56	9.8	10.25	5.82	8.56	7.49	15.59	10.13	8.07	**8.08686**	8hr
6	21	662.6	538	10818	185072	**16**	87.2053	8.44	9.73	10.26	5.82	8.56	7.48	15.6	10.14	8.07	**8.083416**	8hr
6	21	662.6	538	10818	185072	**15**	1.2661	8.36	9.67	10.26	5.82	8.56	7.48	15.6	10.13	8.06	**8.080314**	8hr
7	24	733.2	908	11717	191620	**21**	1.8096	5.57	6.04	13.9	9.74	12.31	5.67	24.88	8.89	7.82	**7.820815**	8hr
7	24	733.2	908	11717	191620	**20**	1.8021	5.4	5.9	13.94	9.72	12.31	5.66	24.92	8.9	7.82	**7.817411**	8hr
7	24	733.2	908	11717	191620	**19**	1.7765	5.32	5.84	13.95	9.71	12.31	5.65	24.91	8.9	7.81	**7.814473**	8hr

Table 4.4: Deviation from Prescribed dose for Patients and ROIs after 8 hours

Figure 4.7 shows the difference in average deviation for models ran for both 40 hours and 8 hours. Although the gap reduces with more runtime, the actual improvement in deviation between these two solutions is relatively small. However, some models are not able to reach a sufficiently small gap after this time. Notably, the largest model, patient 8, was not able to produce a valid solution within 8 hours.

Sometimes, the smaller tumors are able to reach a very small gap. However, this trend is not consistent, since tumor 6 has a very large gap for a smaller number of spheres but a good gap when the number of spheres increases. Furthermore, patient 5 reaches a much larger gap than patient 7, despite the fact that patient 7 is much larger. These inconsistencies highlight the challenges posed by the nonlinearity of integer programming problems.

Chapter 5

Discussion

In this chapter, we review the significance and novelty of our model, provide interpretation of our results, discuss the assumptions and limitations of our modeling framework, and compare our methodology with existing techniques.

Current SFRT treatment planning relies on a treatment planner placing spheres in a square grid-pattern within the tumor. This process has not been optimized or automated, so the number of spheres placed can vary widely between treatment planners. We have designed a mathematical program that both automates the placement of radiation spheres within the tumor and finds the sphere placement that results in a radiation delivery that least deviates from the prescribed dose. This results in less radiation delivery to healthy tissues and more radiation delivery to cancerous tissues.

Our model can create sphere placements for different numbers of spheres (values of ϕ) that treatment planers can use to identify the best spheres to place. They can then fine tune these sphere placements using their expertise in order to provide the best quality care and improve patient quality of life by maximizing tumor reduction and minimizing side effects.

5.1 Interpretation of Results

The visualizations generated from the toy model demonstrate the effectiveness of our model and its ability to place various numbers of spheres within the tumor, accounting for multiple types of dose constraints and prescriptions. They effectively demonstrate the flexibility that

our model provides by allowing the spheres to reposition inside of the tumor to reduce dose delivered to sensitive tissues.

The PortPy results demonstrate the model's scalability to real, three-dimensional tumors that are candidates for SFRT treatment. These models result in quality treatment plans that minimize deviation from the prescribed dose. The PortPy patients experience an increase in average deviation as the number of spheres increases. These conflicting objectives emphasize the need for expert treatment planners that can determine the best final treatment plan that properly balances the needs of the patient.

Most OARs did not experience a clear correlation with the number of nodes placed. This can be explained by the model's ability to adapt to a changing prescription by shifting dose from one OAR to another to better meet the demands of the prescription and constraints.

5.2 Time Considerations

Due to the possibility of rapid degradation of patient health due to delays in treatment, we must consider the requisite runtime for both the model and model construction to determine the usefulness of this tool. The optimization model is not the only time-intensive step. After the ROIs have been properly contoured and the relevant constraints and prescriptions have been determined, the graph must be constructed and the D and A matrices must be constructed. Thankfully, all operations involved problem construction are polynomially bounded, but this does not prevent difficulty. Graph construction for the MIS problem is very fast, often done in seconds, but if the graph were to be constructed at a finer granularity, this problem could easily take hours for large tumors. Early on in the research, the MIS problem was solved for a large tumor that with a grid granularity of 1 mm (as opposed to the current plan of 1 cm). Merely the construction of the graph took over 12 hours and the optimization was not able to reach a reasonable optimality gap within 48 hours. However, we were not able to successfully and meaningfully implement parallel processing of the model parameters, possibly hindered by the Python global interpreter lock, so a properly parallelized script running on a fast computer, especially utilizing a GPU, should be able to perform these operations much faster. However, the optimization model does employ parallel processing, and so with the possible exception of better GPU utilization, the optimization step is unlikely to improve significantly in speed without the use of Heuristics, Decomposition Techniques, or targeted search of the Branch and Bound Tree.

The rest of the parameter construction times will scale similarly to the size of the graph. In our experiments, the graph construction was one of the fastest steps. A maximum independent set was often found in less than a minute for all except the largest tumors, and after 10 minutes a quality solution was found in all cases. The two greatest preprocessing tasks were the creation of the A and D matrices. These are both very large and take significant amounts of time to solve, ranging from half an hour to nearly 8 hours to calculate both matrices for these patients. The A matrix is a product of the PortPy library, so the amount of time it takes to create is fully dictated by the speed of PortPy. We calculate the D matrix from scratch, and its construction time is most significantly affected by the number of points used to discretize each voxel. If more points are used to more accurately determine what percentage of each sphere lies in each voxel, the construction of the D matrix will take significantly more time.

Lastly, we ran our experiments in parallel, meaning that optimization models for all three numbers of sphere placements ran concurrently for 40 hours. If this is a feasible option, this will dramatically improve the process, and, given enough threads and the requisite licenses (Gurobi, the optimization solver, requires a license with a limited number of concurrent sessions), a wide variety of sphere placements could be solved to provide a better starting place for treatment planners.

5.3 Comparison with Existing Techniques

As mentioned in the introduction, there exists one peer reviewed paper that attempts to optimize sphere placement in SFRT [53]. Their goal is the same as ours: to find the best placement of spheres that minimizes deviation from the target dose. However, their model is more restrictive than ours. It takes a fixed sphere placement as an input and allows the entire grid to shift into whatever position will minimize deviation from the target dose. Our model is more flexible and allows spheres to be placed in any configuration within the tumor discretization.

5.4 Limitations and Future Work

Since little work has been done in the optimization community to optimize SFRT sphere placement, there is a significant ammount of work that can still be done in the field.

Parallelization and Speed: As mentioned in the discussion, the preprocessing phase for these models can be very time consuming, but they are not yet maximally efficient. These preprocessing steps could be massively sped up with the help of parallelization. Furthermore, if the ingest pipeline was smoother: if the CT scan was discretized into Voxels in our code, and the A matrix was calculated in our code, the voxels could be made to line up with the sphere centers. This would eschew the need for calculation of the proportion of voxel that lies in a sphere, since this could be calculated once for a single sphere and the voxels surround it and repeated for every candidate sphere for all voxels not bordering the tumor. This would significantly speed up the calculation of the D matrix. If completed, this would only require a single pass through the set of all nodes, with complex distance calculations only performed for voxels on the tumor border. Additionally, various decomposition methods and heuristics could be implemented to speed up the optimization. This would provide faster turn around time of treatment plans in order to ensure a seamless treatment planning process and shorter delays between diagnosis and treatment.

Curated Set of Beams: Current fluence map models in clinical use employ a continuous (or very finely discretized) set of beam angles in order to provide precise beamlet optimization and treatment. Our model relies on the treatment planner determining a set of high quality angles that are likely to result in quality treatment plans. To mitigate this, after our optimal solution is found, the resultant sphere placements could be put into standard software for clinical treatment planning, as this would fully use the full set of feasible beams to ensure that quality beamlet intensities are used.

Downsampling of Voxels: To reduce the size of the model, our voxels were downsampled and enlarged. This reduces the precision of the model significantly. Similar to concerns over the set of beams, one potential solution would be to take the results of the sphere placements from our proposed model and place these spheres within the state-of-the-art treatment planning systems in clinical use. This should reduce bias inherent in the downsampling process.

Untie from PortPy: Currently, our methodology is unable to function without the PortPy library, and PortPy only works on patients within the PortPy library. The primary element

that PortPy provides is the A matrix. This matrix has not been easily found anywhere within the standard clinical treatment planning software, or within other open-source libraries, but it can certainly be calculated. For this model to be used clinically, either the A matrix must be calculated locally or PortPy needs to expand to allow for new patients.

Radio-biological Implementation: Our model does not account for any actual tumor reduction. It only accounts for radiation delivery to the ROIs. A more effective model would be able to predict actual tumor reduction by modeling cellular decay using something like the LQ model [33].

SFRT Quality Metrics: Since the biological effect of SFRT is still an active area of research, it is still uncertain whether one sphere placement pattern will result in greater tumor reduction than another. Thus, our assumption is that more radiation delivered to the tumor will result in more tumor reduction, but it is possible that the tightness of the sphere placement has a role in tumor reduction as well. Future research could evaluate various sphere patterns in order to determine the significance of the effect of various sphere placement patterns, and a future model could account for this metric, potentially using the aggregate distance to the centroid of the spheres as a metric.

Robust Optimization: Robust optimization is commonly employed in radiation therapy treatment planning to accommodate for body movement during radiation delivery. Motion occurs both during and across treatment sessions. During a treatment session, the patient breathes and moves slightly, which can introduce variability into the dose delivery. Across treatment sessions the tumor will shrink. CT scans can deliver a significant dose of radiation, and, coupled with the cost and time requirements, imaging is generally not done between treatment sessions, and if it is done, it is done strategically and sparingly. Thus, one treatment plan is developed and delivered to the patient across multiple sessions. The tumor will shrink during this time, so robust optimization models are often employed in order to account for the possible locations of the tumor as treatment goes on. However, this optimization may be difficult because our model has integer variables. This prohibits the use of the standard L-shaped method. However, SFRT is often done in fewer sessions than conventional radiation therapy due to its use in shrinking tumors before other treatment modalities are administered, so tumor shrinkage may not be as significant of a factor.

Chapter 6

Conclusion

In this thesis, we proposed a new model that combines SFRT sphere placement with fluence map optimization in order to create a robust and flexible framework for determining optimal sphere placement. While existing SFRT implementations have shown promise in treating large or bulky tumors, our proposed model is one of the first optimal implementations of SFRT that computes optimal radiation sphere locations, aiming at minimizing the damage to healthy tissues while maximizing the dose to the tumor. Our model integrates computationally-tractable linear fluence optimization models with a new sphere placement modeling technique rooted in the integer programming formulation of the maximum independent set problem.

To demonstrate the efficacy of our proposed methods, we have used an de-identified publicly available medical images from the The Cancer Imaging Archive, a National Cancer Institute-funded service. We have utilized discretization methods to represent the tumor based on real imaging of cancer patients and have tested multiple implementations of the MIS problem across several tumor discretization techniques in order to determine the best SFRT sphere locations. Furthermore, we have developed an integrated model that derives the SFRT treatment plan using fluence map optimization while simultaneously determining the placement of the maximum number of spheres. This ensures that the resultant sphere placement minimizes damage to healthy tissues.

Future works of this thesis can consider optimization models that integrate radio-biological outcomes of treatment. Further, the models developed in this thesis can be extended to consider specific SFRT quality metrics. While we considered a single-objective implementation of SFRT fluence map optimization with a maximum independent set, more complex models (such as robust optimization) models may be considered.

Our model and experimental results provide a higher level of confidence in SFRT treatment planning by providing mathematical certainty of sphere placement quality. This aims to provide greater consistency in patient outcomes so that the clinical and scientific community can better prescribe and research SFRT. This model is one more measure that can provide cancer patients with confidence and peace of mind that they are receiving the best possible care in one of the most difficult times in a patient's life.

Bibliography

[1] MSK Radiation Therapy: Timeline of Progress | Memorial Sloan Kettering Cancer Center, . URL https://www.mskcc.org/timeline/msk-radiation-therapy-timeline-progress.

[2] (PDF) Understanding Breast Cancer – The long and winding road. *ResearchGate*, . doi: 10.1016/j.bbacli.2017.01.001. URL https://www.researchgate.net/publication/313020660_Understanding_Breast_Cancer_-_The_long_and_winding_road.

[3] (PDF) Dosimetric Comparison of the Simultaneous Integrated Boost in Whole-Breast Irradiation after Breast-Conserving Surgery: IMRT, IMRT plus an Electron Boost and VMAT. *ResearchGate*, . doi: 10.1371/journal.pone.0120811. URL https://www.researchgate.net/publication/273955412_Dosimetric_Comparison_of_the_Simultaneous_Integrated_Boost_in_Whole-Breast_Irradiation_after_Breast-Conserving_Surgery_IMRT_IMRT_plus_an_Electron_Boost_and_VMAT.

[4] *The Edwin Smith surgical papyrus: published in facsimile and hieroglyphic transliteration with translation and commentary in two volumes*. The University of Chicago Oriental Institute publications. Univ. of Chicago Press, Chicago, Ill., 1930.

[5] Noga Alon, László Babai, and Alon Itai. A fast and simple randomized parallel algorithm for the maximal independent set problem. *Journal of Algorithms*, 7(4):567–583, December 1986. ISSN 0196-6774. doi: 10.1016/0196-6774(86)90019-2. URL https://www.sciencedirect.com/science/article/pii/0196677486900192.

[6] Agnes Arnold-Forster. A pathology of progress? Locating the historiography of cancer. *The British Journal for the History of Science*, 49(4):627–634, December 2016. ISSN 0007-0874, 1474-001X. doi: 10.1017/S0007087416001175. URL https://www.cambridge.org/core/journals/british-journal-for-the-history-of-science/article/abs/pathology-of-progress-locating-the-historiography-of-cancer/1B685127054533F238801064AA49F123.

[7] Rajamanickam Baskar, Kuo Ann Lee, Richard Yeo, and Kheng-Wei Yeoh. Cancer and Radiation Therapy: Current Advances and Future Directions. *International Journal of Medical Sciences*, 9(3):193–199, February 2012. ISSN 1449-1907. doi: 10.7150/ijms.3635. URL https://www.ncbi.nlm.nih.gov/pmc/articles/PMC3298009/.

[8] Jacques Bernier, Eric J. Hall, and Amato Giaccia. Radiation oncology: a century of achievements. *Nature Reviews Cancer*, 4(9):737–747, September 2004. ISSN 1474-1768. doi: 10.1038/nrc1451. URL https://www.nature.com/articles/nrc1451. Publisher: Nature Publishing Group.

[9] Cole Billena and Atif J. Khan. A Current Review of Spatial Fractionation: Back to the Future? *International Journal of Radiation Oncology*Biology*Physics*, 104 (1):177–187, May 2019. ISSN 0360-3016. doi: 10.1016/j.ijrobp.2019.01.073. URL https://www.sciencedirect.com/science/article/pii/S0360301619301543.

[10] Freddie Bray, Mathieu Laversanne, Hyuna Sung, Jacques Ferlay, Rebecca L. Siegel, Isabelle Soerjomataram, and Ahmedin Jemal. Global cancer statistics 2022: GLOBOCAN estimates of incidence and mortality worldwide for 36 cancers in 185 countries. *CA: A Cancer Journal for Clinicians*, 74(3):229–263, 2024. ISSN 1542-4863. doi: 10.3322/caac.21834. URL https://onlinelibrary.wiley.com/doi/abs/10.3322/caac.21834. _eprint: https://onlinelibrary.wiley.com/doi/pdf/10.3322/caac.21834.

[11] Sergiy Butenko. *Maximum independent set and related problems, with applications*. Ph.D., University of Florida, United States – Florida, 2003. URL https://www.proquest.com/docview/305325666/abstract/59C71DC4EEDC4D3EPQ/1. ISBN: 9780496674725.

[12] Thorsten M Buzug. Computed tomography. In *Springer handbook of medical technology*, pages 311–342. Springer, 2011.

[13] W. F. Bynum and Roy Porter. *Medicine and the Five Senses*. Cambridge University Press, February 1993. ISBN 978-0-521-36114-9. Google-Books-ID: iOw8N6FAqNAC.

[14] Bruce A. Chabner and Thomas G. Roberts. Chemotherapy and the war on cancer. *Nature Reviews Cancer*, 5(1):65–72, January 2005. ISSN 1474-1768. doi: 10.1038/nrc1529. URL https://www.nature.com/articles/nrc1529. Publisher: Nature Publishing Group.

[15] Cyrus Chargari, Eric Deutsch, Pierre Blanchard, Sebastien Gouy, Hélène Martelli, Florent Guérin, Isabelle Dumas, Alberto Bossi, Philippe Morice, Akila N. Viswanathan, and Christine Haie-Meder. Brachytherapy: An overview for clinicians. *CA: A Cancer Journal for Clinicians*, 69(5):386–401, 2019. ISSN 1542-4863. doi: 10.3322/caac.21578.

URL https://onlinelibrary.wiley.com/doi/abs/10.3322/caac.21578. _eprint: https://onlinelibrary.wiley.com/doi/pdf/10.3322/caac.21578.

[16] Bhupender S. Chhikara and Keykavous Parang. Global Cancer Statistics 2022: the trends projection analysis. *Chemical Biology Letters*, 10(1):451–451, January 2023. ISSN 2347-9825. doi: https://scholar.google.com/scholar?q=urn:nbn:sciencein.cbl.2023.v10.451. URL https://pubs.thesciencein.org/journal/index.php/cbl/article/view/451. Number: 1.

[17] Lisa Deloch, Anja Derer, Josefin Hartmann, Benjamin Frey, Rainer Fietkau, and Udo S. Gaipl. Modern Radiotherapy Concepts and the Impact of Radiation on Immune Activation. *Frontiers in Oncology*, 6, June 2016. ISSN 2234-943X. doi: 10.3389/fonc.2016.00141. URL https://www.frontiersin.org/journals/oncology/articles/10.3389/fonc.2016.00141/full. Publisher: Frontiers.

[18] Matthias Ehrgott, Çiğdem Güler, Horst W. Hamacher, and Lizhen Shao. Mathematical optimization in intensity modulated radiation therapy. *Annals of Operations Research*, 175(1):309–365, March 2010. ISSN 1572-9338. doi: 10.1007/s10479-009-0659-4. URL https://doi.org/10.1007/s10479-009-0659-4.

[19] Luca Falzone, Salvatore Salomone, and Massimo Libra. Evolution of Cancer Pharmacological Treatments at the Turn of the Third Millennium. *Frontiers in Pharmacology*, 9, November 2018. ISSN 1663-9812. doi: 10.3389/fphar.2018.01300. URL https://www.frontiersin.org/journals/pharmacology/articles/10.3389/fphar.2018.01300/full. Publisher: Frontiers.

[20] Michael Galetzka and Patrick O. Glauner. A Simple and Correct Even-Odd Algorithm for the Point-in-Polygon Problem for Complex Polygons, July 2017. URL http://arxiv.org/abs/1207.3502. arXiv:1207.3502 [cs].

[21] Somayeh Gholami, Hassan Ali Nedaie, Francesco Longo, Mohammad Reza Ay, Stacey Wright, and Ali S. Meigooni. Is grid therapy useful for all tumors and every grid block design? *Journal of Applied Clinical Medical Physics*, 17(2):206–219, 2016. ISSN 1526-9914. doi: 10.1120/jacmp.v17i2.6015. URL https://onlinelibrary.wiley.com/doi/abs/10.1120/jacmp.v17i2.6015. _eprint: https://onlinelibrary.wiley.com/doi/pdf/10.1120/jacmp.v17i2.6015.

[22] Vineet Goel and Amar Mukherjee. An optimal parallel algorithm for volume ray casting. *The Visual Computer*, 12(1):26–39, January 1996. ISSN 1432-2315. doi: 10.1007/BF01782217. URL https://doi.org/10.1007/BF01782217.

[23] Steven I. Hajdu and Manjunath Vadmal. A note from history: Landmarks in history of cancer, Part 6. *Cancer*, 119(23):4058–4082, 2013. ISSN 1097-0142. doi: 10.1002/cncr.28319. URL https://onlinelibrary.wiley.com/doi/abs/10.1002/cncr.28319. _eprint: https://onlinelibrary.wiley.com/doi/pdf/10.1002/cncr.28319.

[24] Kai Hormann and Alexander Agathos. The point in polygon problem for arbitrary polygons. *Computational Geometry*, 20(3):131–144, November 2001. ISSN 0925-7721. doi: 10.1016/S0925-7721(01)00012-8. URL https://www.sciencedirect.com/science/article/pii/S0925772101000128.

[25] Richard M Karp. Reducibility among combinatorial problems. In *50 Years of Integer Programming 1958-2008: from the Early Years to the State-of-the-Art*, pages 219–241. Springer, 2009.

[26] A. Karpozilos and N. Pavlidis. The treatment of cancer in Greek antiquity. *European Journal of Cancer*, 40(14):2033–2040, September 2004. ISSN 0959-8049. doi: 10.1016/j.ejca.2004.04.036. URL https://www.sciencedirect.com/science/article/pii/S0959804904004162.

[27] Daniela S. Krause and Richard A. Van Etten. Tyrosine Kinases as Targets for Cancer Therapy. *New England Journal of Medicine*, 353(2):172–187, July 2005. ISSN 0028-4793. doi: 10.1056/NEJMra044389. URL https://www.nejm.org/doi/full/10.1056/NEJMra044389. Publisher: Massachusetts Medical Society _eprint: https://www.nejm.org/doi/pdf/10.1056/NEJMra044389.

[28] Andrzej Kułakowski. The contribution of Marie Skłodowska-Curie to the development of modern oncology. *Analytical and Bioanalytical Chemistry*, 400(6):1583–1586, June 2011. ISSN 1618-2650. doi: 10.1007/s00216-011-4712-1. URL https://doi.org/10.1007/s00216-011-4712-1.

[29] George E. Laramore. Role of particle radiotherapy in the management of head and neck cancer. *Current Opinion in Oncology*, 21(3):224, May 2009. ISSN 1040-8746. doi: 10.1097/CCO.0b013e328329b716. URL https://journals.lww.com/co-oncology/abstract/2009/05000/role_of_particle_radiotherapy_in_the_management_of.8.aspx.

[30] L. Larrea, V. Gonzalez, P. Antonini, E. Lopez, and M. C. Banos. Lattice Radiotherapy (LRT)-Spatially Fractionated Radiotherapy (SFRT): Advanced Non-Small Cell Lung Cancer (NSCLC): Early Experience. *International Journal of Radiation Oncology, Biology, Physics*, 111(3):e443, November 2021. ISSN 0360-3016.

doi: 10.1016/j.ijrobp.2021.07.1253. URL https://www.redjournal.org/article/S0360-3016(21)02123-4/fulltext. Publisher: Elsevier.

[31] Mauro Loi, Nuyttens , Joost J, Desideri , Isacco, Greto , Daniela, , and Lorenzo Livi. Single-Fraction Radiotherapy (SFRT) For Bone Metastases: Patient Selection And Perspectives. *Cancer Management and Research*, 11:9397–9408, November 2019. ISSN null. doi: 10.2147/CMAR.S186630. URL https://www.tandfonline.com/doi/abs/10.2147/CMAR.S186630. Publisher: Dove Medical Press _eprint: https://www.tandfonline.com/doi/pdf/10.2147/CMAR.S186630.

[32] M Luby. A simple parallel algorithm for the maximal independent set problem. In *Proceedings of the seventeenth annual ACM symposium on Theory of computing - STOC '85*, pages 1–10, Providence, Rhode Island, United States, 1985. ACM Press. ISBN 978-0-89791-151-1. doi: 10.1145/22145.22146. URL http://portal.acm.org/citation.cfm?doid=22145.22146.

[33] Stephen Joseph McMahon. The linear quadratic model: usage, interpretation and challenges. *Physics in Medicine & Biology*, 64(1):01TR01, December 2018. doi: 10.1088/1361-6560/aaf26a. URL https://dx.doi.org/10.1088/1361-6560/aaf26a. Publisher: IOP Publishing.

[34] Edmund S. Meltzer and Gonzalo M. Sanchez. The Edwin Smith Papyrus : Updated Translation of the Trauma Treatise and Modern Medical Commentaries. pages 1–400, 2014. URL https://www.torrossa.com/it/resources/an/5263697. Publisher: Lockwood Press.

[35] Mohammed Mohiuddin, William F. Regine, and Gerald Marks. Prognostic significance of tumor fixation of rectal carcinoma: Implications for adjunctive radiation therapy. *Cancer*, 78(4):717–722, 1996. ISSN 1097-0142. doi: 10.1002/(SICI)1097-0142(19960815)78:4<717::AID-CNCR4>3.0.CO;2-B. URL https://onlinelibrary.wiley.com/doi/abs/10.1002/%28SICI%291097-0142%2819960815%2978%3A4%3C717%3A%3AAID-CNCR4%3E3.0.CO%3B2-B. _eprint: https://onlinelibrary.wiley.com/doi/pdf/10.1002/%28SICI%291097-0142%2819960815%2978%3A4%3C717%3A%3AAID-CNCR4%3E3.0.CO%3B2-B.

[36] John E. Moulder, , and Colin Seymour. Radiation fractionation: the search for isoeffect relationships and mechanisms. *International Journal of Radiation Biology*, 94(8):743–751, July 2018. ISSN 0955-3002. doi: 10.1080/09553002.2017.1376764. URL https:

//doi.org/10.1080/09553002.2017.1376764. Publisher: Taylor & Francis _eprint: https://doi.org/10.1080/09553002.2017.1376764.

[37] Siddhartha Mukherjee. *The Emperor of All Maladies: A Biography of Cancer*. Simon and Schuster, November 2010. ISBN 978-1-4391-8171-3.

[38] Don K. Nakayama and Patrick C. Bonasso. The History of Multimodal Treatment of Wilms' Tumor. *The American Surgeon™*, 82(6):487–492, June 2016. ISSN 0003-1348. doi: 10.1177/000313481608200607. URL https://doi.org/10.1177/000313481608200607. Publisher: SAGE Publications.

[39] CF Njeh. Tumor delineation: The weakest link in the search for accuracy in radiotherapy. *Journal of medical physics*, 33(4):136–140, 2008.

[40] World Health Organization et al. Technical specifications of radiotherapy equipment for cancer treatment. In *Technical specifications of radiotherapy equipment for cancer treatment*. 2021.

[41] Niki Papavramidou, Theodossis Papavramidis, and Thespis Demetriou. Ancient Greek and Greco–Roman Methods in Modern Surgical Treatment of Cancer. *Annals of Surgical Oncology*, 17(3):665–667, March 2010. ISSN 1534-4681. doi: 10.1245/s10434-009-0886-6. URL https://doi.org/10.1245/s10434-009-0886-6.

[42] H. Edwin Romeijn, Ravindra K. Ahuja, James F. Dempsey, Arvind Kumar, and Jonathan G. Li. A novel linear programming approach to fluence map optimization for intensity modulated radiation therapy treatment planning. *Physics in Medicine & Biology*, 48(21):3521, October 2003. ISSN 0031-9155. doi: 10.1088/0031-9155/48/21/005. URL https://dx.doi.org/10.1088/0031-9155/48/21/005.

[43] Gopal B Saha and B Gopal. *Basics of PET imaging: physics, chemistry, and regulations*. Springer, 2005.

[44] Abbas Musleh Salman and Ahmed Sabah Al-Jilawi. Applications of maximum independent set. *AIP Conference Proceedings*, 2398(1):060015, October 2022. ISSN 0094-243X. doi: 10.1063/5.0093375. URL https://doi.org/10.1063/5.0093375.

[45] Daniela Schulz-Ertner and Hirohiko Tsujii. Particle Radiation Therapy Using Proton and Heavier Ion Beams. *Journal of Clinical Oncology*, 25(8):953–964, March 2007. ISSN 0732-183X. doi: 10.1200/JCO.2006.09.7816. URL https://ascopubs.org/doi/full/10.1200/JCO.2006.09.7816. Publisher: Wolters Kluwer.

[46] Rebecca L. Siegel, Tyler B. Kratzer, Angela N. Giaquinto, Hyuna Sung, and Ahmedin Jemal. Cancer statistics, 2025. *CA: A Cancer Journal for Clinicians*, 75(1):10–45, 2025. ISSN 1542-4863. doi: 10.3322/caac.21871. URL https://onlinelibrary.wiley.com/doi/abs/10.3322/caac.21871. _eprint: https://onlinelibrary.wiley.com/doi/pdf/10.3322/caac.21871.

[47] C. R. I. Staff. Exploring the Different Types of Cancer and Treatment Options, December 2023. URL https://www.cancerresearch.org/blog/exploring-the-different-types-of-cancer-and-treatment-options.

[48] Akulapalli Sudhakar. History of Cancer, Ancient and Modern Treatment Methods. *Cancer Science & Therapy*, 01(02):i–iv, 2009. doi: 10.4172/1948-5956.100000e2. URL https://hal.science/hal-04693396. Publisher: Omics Publishing Group.

[49] Robert Endre Tarjan and Anthony E. Trojanowski. Finding a Maximum Independent Set. *SIAM Journal on Computing*, July 2006. doi: 10.1137/0206038. URL https://epubs.siam.org/doi/10.1137/0206038. Publisher: Society for Industrial and Applied Mathematics.

[50] Gregory Tsoucalas and Markos Sgantzos. Hippocrates (ca 460-370 BC) on nasal cancer.

[51] Dominik Weishaupt, Victor D Köchli, Borut Marincek, Johannes M Froehlich, Daniel Nanz, and Klaas P Pruessmann. *How does MRI work?: an introduction to the physics and function of magnetic resonance imaging*, volume 2. Springer, 2006.

[52] Weisi Yan, Mohammad K. Khan, Xiaodong Wu, Charles B. Simone, Jiajin Fan, Eric Gressen, Xin Zhang, Charles L. Limoli, Houda Bahig, Slavisa Tubin, and Waleed F. Mourad. Spatially fractionated radiation therapy: History, present and the future. *Clinical and Translational Radiation Oncology*, 20:30–38, January 2020. ISSN 2405-6308. doi: 10.1016/j.ctro.2019.10.004. URL https://www.sciencedirect.com/science/article/pii/S2405630819301041.

[53] Weijie Zhang, Yuting Lin, Fen Wang, Rajeev Badkul, Ronald C. Chen, and Hao Gao. Lattice position optimization for LATTICE therapy. *Medical Physics*, 50(12):7359–7367, 2023. ISSN 2473-4209. doi: 10.1002/mp.16572. URL https://onlinelibrary.wiley.com/doi/abs/10.1002/mp.16572. _eprint: https://onlinelibrary.wiley.com/doi/pdf/10.1002/mp.16572.

[54] Miloš Šrámek. 20 years of volume rendering. In *Proceedings of the 22nd Spring Conference on Computer Graphics*, SCCG '06, pages 7–16, New York, NY, USA, April 2006.

Association for Computing Machinery. ISBN 978-1-4503-2829-6. doi: 10.1145/2602161.2602162. URL https://doi.org/10.1145/2602161.2602162.